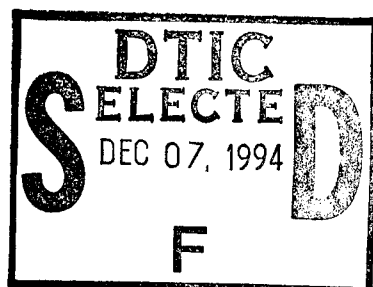


NPS-EC-93-018

NAVAL POSTGRADUATE SCHOOL

Monterey, California



**Application of the Measured Equation of
Invariance to Wave Propagation over
Irregular, Inhomogeneous Terrain**

by

Ramakrishna Janaswamy

October 1993

Approved for public release; distribution unlimited.

Prepared for: Naval Postgraduate School, Monterey, CA

19941201 079

Naval Postgraduate School
Monterey, California 93943-5000

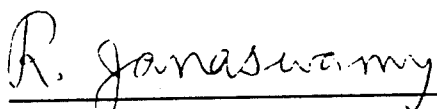
Rear Admiral T. A. Mercer
Superintendent

H. Shull
Provost

This report was prepared and funded by the Naval Security Group Command.

Reproduction of all or part of this report is authorized.

This report was prepared by:



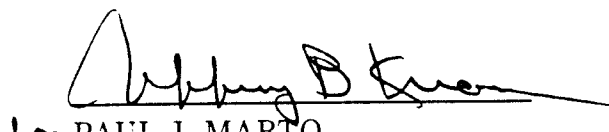
RAMAKRISHNA JANASWAMY
Associate Professor,
Department of Electrical and
Computer Engineering

Reviewed by:

Released by:



MICHAEL A. MORGAN
Chairman,
Department of Electrical and
Computer Engineering


for PAUL J. MARTO
Dean of Research

REPORT DOCUMENTATION PAGE

Form Approved
OMB No. 0704-0188

Public reporting burden for this collection of information is estimated to average 1 hour per response, including the time for reviewing instructions, searching existing data sources, gathering and maintaining the data needed, and completing and reviewing the collection of information. Send comments regarding this burden estimate or any other aspect of this collection of information, including suggestions for reducing this burden, to Washington Headquarters Services, Directorate for Information Operations and Reports, 1215 Jefferson Davis Highway, Suite 1204, Arlington, VA 22202-4302, and to the Office of Management and Budget, Paperwork Reduction Project (0704-0188), Washington, DC 20503.

1. AGENCY USE ONLY (Leave blank)		2. REPORT DATE October 1993		3. REPORT TYPE AND DATES COVERED Technical Report 1 Oct 92-1 Oct 93	
4. TITLE AND SUBTITLE Application of the Measured Equation of Invariance to Wave Propagation over Irregular, Inhomogeneous Terrain				5. FUNDING NUMBERS	
6. AUTHOR(S) Ramakrishna Janaswamy					
7. PERFORMING ORGANIZATION NAME(S) AND ADDRESS(ES) Naval Postgraduate School Monterey, CA 93943-5000				8. PERFORMING ORGANIZATION REPORT NUMBER NPS-EC-93-018	
9. SPONSORING / MONITORING AGENCY NAME(S) AND ADDRESS(ES) Naval Security Group Command Naval Security Group Support Activity 3801 Nebraska Avenue NW Washington DC 20393-5220				10. SPONSORING / MONITORING AGENCY REPORT NUMBER	
11. SUPPLEMENTARY NOTES The views expressed in this report are those of the authors and do not reflect the official policy or position of the Department of Defense or the United States Government.					
12a. DISTRIBUTION / AVAILABILITY STATEMENT Approved for public release; distribution is unlimited.				12b. DISTRIBUTION CODE	
13. ABSTRACT (Maximum 200 words) The problem of propagation of electromagnetic waves over irregular, inhomogeneous terrain is solved by a finite difference scheme. The method is fast and requires considerably less memory compared to the integral equation methods. The method requires a storage space of order $O(N)$ and an execution time of order $O(N^2)$. Fields generated by a TE_z line source are represented in an integral form in terms of the field over a flat, constant impedance plane, and the field scattered by the terrain irregularities and inhomogeneities. Accurate expressions are provided for the incident field and the Green's function, whose evaluation is otherwise accomplished by the rather time-consuming Sommerfeld's integrals. Measured equation of invariance is used to terminate the mesh. The sparse matrix generated by the method is inverted using Ricatti transform. Numerical results are presented for the ground wave as well as the sky wave. Comparison is made for known geometries to establish the validity and limitations of the method.					
14. SUBJECT TERMS Electromagnetic Wave Propagation, Terrain Effects, Finite Differences				15. NUMBER OF PAGES 65	
				16. PRICE CODE	
17. SECURITY CLASSIFICATION OF REPORT UNCLASSIFIED	18. SECURITY CLASSIFICATION OF THIS PAGE UNCLASSIFIED	19. SECURITY CLASSIFICATION OF ABSTRACT UNCLASSIFIED	20. LIMITATION OF ABSTRACT SAR		

Abstract: Propagation of electromagnetic waves over irregular, inhomogeneous terrain is solved by a finite difference scheme. The method is fast and requires considerably less memory than the integral equation methods. The method requires a storage space of order $O(N)$ and an execution time of order $O(N^2)$. Fields generated by a TE_z line source are represented in an integral form in terms of the field over a flat, constant impedance plane, and the field scattered by the terrain irregularities and inhomogeneities. Accurate expressions are provided for the incident field and the Green's function, whose evaluation is otherwise accomplished by the rather time-consuming Sommerfeld's integrals. Measured equation of invariance is used to terminate the mesh. The sparse matrix generated by the method is inverted by the Ricatti transform. Numerical results are presented for the ground wave as well as the sky wave. Comparison is made for known geometries to establish the validity and limitations of the method.

Accession For	
NTIS CRA&I	<input checked="" type="checkbox"/>
DTIC TAB	<input type="checkbox"/>
Unannounced	<input type="checkbox"/>
Justification	
By	
Distribution/	
Availability Codes	
Dist	Avail and/or Special
A-1	

I. INTRODUCTION

Electromagnetic wave propagation over hilly terrain is important not only in point-to-point communication over land, but also in ground-to-air communication. Of late, it has assumed importance in outdoor propagation in the context of personal communications network design. An exact analytical solution of the problem for general terrain is not possible and one often resorts to an approximate or a numerical approach. In a previous paper [1], we developed a numerical model for propagation predictions over inhomogeneous, irregular terrain using the magnetic field integral equation. Although the method could include all effects of wave propagation such as reflection, diffraction, surface wave excitation, and backscattering, a principal limitation of the method was the requirement of large computer resources (CPU time and memory), particularly for electrically large terrain irregularities. For instance, if the integral equation is solved numerically by the method of moments [2], the matrix fill time would be of order $O(N^2)$ and the inversion time of order $O(N^3)$, where N is the total number of unknowns. As the matrix generated is dense, the memory requirements would be of order $O(N^2)$. The method is attractive for small terrain irregularities, but is computationally prohibitive for large terrain irregularities [1].

In this paper we present a computationally efficient model of wave propagation based on finite differences. It may be noted that this method has no semblance to the one proposed in [3], where one proceeds with the parabolic equation approximation of the Helmholtz equation. Use of parabolic equation approximation precludes backscattering, which is sometimes important. In contrast, we apply finite differences directly to the Helmholtz equation without introducing any dubious approximations. Even though one has to handle a larger matrix when dealing with finite differences in contrast to boundary methods such as integral equation methods, the resulting matrix is sparse, and often faster to invert than the dense matrix generated via the latter. The matrix fill time is still of order $O(N^2)$, but the inversion time is reduced to a lower order of $O(N)$. Thus, the real advantage of a finite difference scheme is felt for large problems where the run time is dominated by the inversion time. Substantial savings in memory are also accomplished as the matrix is sparse. The memory required is only of order $O(N)$. The method can potentially solve larger problems than possible with the method of moments. The principal

difficulty associated with the use of finite differences is the treatment of mesh truncation when applied to open type of problems such as encountered in propagation, antennas, and scattering. We will use a method known as the Measured Equation of Invariance (MEI) originally proposed by Mei, *et al.*, [4] to treat the mesh truncation.

The term *scatterer* will be used generically to denote an obstacle in an open environment. Local radiation conditions such as those proposed in [5] and [6] are good when the truncating boundary is far removed so that it is in the far-zone field. However, this results in a larger matrix size with obvious implications to computational time and memory. Global type radiation conditions [7] can be used on a tighter terminating boundary to result in a smaller computational domain. However, this will destroy the sparsity of the matrix generated by finite differences and defeats the whole purpose of employing it in the first place. What is needed is a local boundary condition of the type in [5], but applicable very close to the scatterer. Although it is far more complex to find near field radiation conditions than it is to find far field ones, it is partially offset by the fact that boundary conditions on a *continuous spatial domain* are not needed when finite methods are used. The MEI method enables one to generate the near-field conditions over a discrete domain.

In this paper we deal with only two-dimensional sources and fields, and one dimensional terrain characteristics. Accordingly, the terrain properties, the sources, and the corresponding fields are all invariant with respect to the longitudinal variable z . It is assumed that the terrain is characterized by its local impedance and height over a reference plane, both of which may vary from point to point. In section IIa, we present a finite difference discretization of the two dimensional Helmholtz equation and present an overview of the present method. To realize the mesh termination conditions via the MEI method described in IIId, an accurate representation of the near-zone scattered field is necessary. In section IIb we give an integral representation of the scattered field of a TE_z line source over an irregular, impedance surface. The corresponding expressions for the incident field and the Green's functions are presented in section IIc. In section IIe, we describe the Riccati block-by-block elimination technique [8] of sparse matrix inversion. Finally in section III we present numerical results for both the sky wave and the ground wave and provide comparisons for test geometries.

II. FORMULATION

In the present paper, we consider a two dimensional situation as shown in Fig. 1. The transmitting antenna is a transversely polarized electric line source located at (x_o, y_o) . Such a source will have its electric field confined to the transverse xy plane, and is the two-dimensional counterpart of the superposition of a vertical electric dipole (VED) and a horizontal electric dipole (HED) in three dimensions. The field due to the source can be classified as TE_z , and all components could be expressed in terms of the z -component, H_z , of the magnetic field. It is assumed that all distance variables are normalized with respect to the free-space wavenumber $k_o = \omega\sqrt{\mu_o\epsilon_o}$, where ω is the radian frequency of the wave, ϵ_o is the permittivity, and μ_o the permeability of free-space. Accordingly, we set $x := k_o x$, $y := k_o y$, etc. An $e^{j\omega t}$ time dependence is assumed and suppressed. For TE_z polarization, the impedance boundary condition [9] of the form $\hat{n} \times \vec{E} = \eta_o \Delta \hat{n} \times (\hat{n} \times \vec{H})$, relating the electric field vector \vec{E} to the magnetic field vector \vec{H} leads to

$$\frac{\partial H_z}{\partial n} = j\Delta H_z, \quad (1)$$

where the unit normal \hat{n} points out of the impedance surface, $\eta_o = \sqrt{\mu_o/\epsilon_o}$ is the intrinsic impedance of free space, and Δ is the normalized impedance of the surface.

IIa. Overview of the Method:

We let ψ to denote the z -component of the scattered magnetic field due to a TE_z line source over an inhomogeneous, irregular terrain. We assume that ψ represents scattering only from the irregularities and inhomogeneities in a reference impedance plane. Thus, the scattered field is identically zero when the terrain is flat having an impedance equal to the reference impedance. The *scatterer* then consists of those portions of the terrain where (i) the impedance is different from the reference value, and (ii) the elevation is different from zero. The computational domain consists of a region in space bounded by the terrain at the bottom and a terminating (*i.e.*, truncating) boundary at the top as shown in Fig. 2. It is assumed that the boundary of the scatterer is subdivided into $N - 1$ segments, thereby, generating N points on it. The terminating boundary is similarly partitioned into $N - 1$ segments. We generate a structured mesh in the computational domain by adding M interior layers between the object boundary and the terminating

boundary, each having N points. A total of $M + 2$ layers, each having N points are thus generated. Layer numbering is done in ascending order starting from the object boundary (layer number 0) and progressing towards the terminating boundary. Node numbering is done from left (number 1) to right (number N). We use the notation (x_m^n, y_m^n) , $m = 0, 1, \dots, M + 1$, $n = 1, \dots, N$ to denote the cartesian coordinates of the n th point on layer number m . Points on the layer immediately following the scatterer are assumed to lie on the local normal emanating from a point on the scatterer. This is to permit easy implementation of the impedance boundary condition of (1). Within the computational domain, the scattered field ψ satisfies the scalar Helmholtz equation

$$\left(\frac{\partial^2}{\partial x^2} + \frac{\partial^2}{\partial y^2} \right) \psi + \psi = 0. \quad (2)$$

Since the terrain irregularities do not necessarily conform to any one standard coordinate system, the mesh is non-orthogonal, and traditional finite difference equations are not applicable. We will develop the required finite difference equations similar to the method outlined in [10]. Prompted by the presence of second order derivatives in the Helmholtz equation, we choose a five-point star mesh centered at $0(X_0, Y_0)$ and surrounded by four neighboring nodes with *local* coordinates (X_k, Y_k) , $k = 1, \dots, 4$, as shown in Fig. 3b. The global indices of the nodes 0, 1, 2, 3, and 4 are (m, n) , $(m - 1, n)$, $(m + 1, n)$, $(m, n - 1)$, and $(m, n + 1)$ respectively. Using the notation in the local coordinates that $\psi_k = \psi(X_k, Y_k)$, we assume a finite difference equation over the mesh in the form

$$\psi_0 + \sum_{k=1}^4 c_k \psi_k = 0, \quad (3)$$

where, c_k , are unknown complex constants. The above equation can be rewritten as

$$\sum_{k=1}^4 c_k \frac{\psi_k}{\psi_0} = -1. \quad (4)$$

The coefficients are determined by choosing four linearly independent plane waves (*i.e.*, trial solutions of (2)) traveling along the lines joining the central node to the four neighboring nodes; *i.e.*, we choose

$$\frac{\psi_k}{\psi_0} = e^{-j d_k \cos(\alpha_k - \alpha_l)}, \quad l = 1, \dots, 4 \quad (5)$$

where (d_k, α_k) are the polar coordinates of the neighboring nodes with respect to the central node 0. The linear system of equations resulting from (4) can then be solved for the unknowns c_k . It is interesting to note that the values for the coefficients reduce to the standard values when the mesh conforms to a standard coordinate system. The computational domain is open ended at the sides and one cannot choose a five-point star mesh as above. At the two ends of the domain, a modified mesh as shown in Figs. 3a and 3c is used. For the mesh shown in Fig. 3a, it is possible that the plane waves traveling along directions 3 and 4 become linearly dependent, or nearly so. To avoid this degeneracy, we reverse the direction of the plane wave traveling along 0 – 3 and solve the linear system. Likewise, to avoid degeneracy with the mesh of Fig. 3c, we reverse the direction of the plane wave traveling along 0 – 4 and solve for the coefficients.

At the lower (object) boundary of the computational domain, the impedance boundary condition (1) is applicable to the total field $H_z = \chi + \psi$, where $\chi = H_{0z}$ is the incident field. For small distances, the solution of (1) along the normal results in

$$\psi_0^n = -\chi_0^n + (\psi_1^n + \chi_1^n)e^{-j\Delta_s^n h_n} \stackrel{\text{def}}{=} -\chi_0^n + (\psi_1^n + \chi_1^n)\beta_n, \quad (6)$$

where $h_n = \sqrt{(x_1^n - x_0^n)^2 + (y_1^n - y_0^n)^2}$ is the normal distance between scatterer and the first interior layer at the n th node, Δ_s^n is the value of Δ_s at the n th node, $\psi_m^n = \psi(x_m^n, y_m^n)$, and $\chi_m^n = \chi(x_m^n, y_m^n)$.

Additional conditions are needed at the artificial, terminating boundary. To simulate free-space, boundary conditions proposed by Mei *et al.*, [4] are assumed to hold on the boundary. Accordingly, on the five-point star mesh of Fig. 3b formed by layer numbers $M - 1$, M , and $M + 1$, the scattered field satisfies (in the local coordinates)

$$\psi_0 + \sum_{k=1}^4 a_k \psi_k = 0, \quad (7)$$

where the complex coefficients a_k are different from c_k . They are determined in a fashion similar to the latter except that the trial solutions are no longer plane waves but are dependent on the geometry of the scatterer and the location of the mesh. Such trial solutions can be obtained from the near-zone behavior of the field and further discussed

in section II d. It is important to note that a discrete equation of the form (7) over a five-point computational molecule of Fig. 3 can only capture spatial derivatives upto second order (without the cross terms). Equations (3), (6) and (7) are combined to result in a matrix equation of the form

$$\mathbf{A}_1 \Psi^3 + \mathbf{B}_1 \Psi^1 + \mathbf{C}_1 \Psi^2 = \mathbf{F}^1 \quad (8)$$

$$\mathbf{A}_n \Psi^{n-1} + \mathbf{B}_n \Psi^n + \mathbf{C}_n \Psi^{n+1} = \mathbf{F}^n, \quad 2 \leq n \leq N-1 \quad (9)$$

$$\mathbf{A}_N \Psi^{N-1} + \mathbf{B}_N \Psi^N + \mathbf{C}_N \Psi^{N-2} = \mathbf{F}^N, \quad (10)$$

where $\Psi^n = [\psi_1^n, \psi_2^n, \dots, \psi_M^n]^t$ is the column vector of unknown values on the M interior layers at the node n , $\mathbf{A}_n, \mathbf{B}_n, \mathbf{C}_n$ are banded matrices of order $M \times M$ given by

$$\mathbf{A}_n = \begin{pmatrix} c_3^{2,n} & 0 & \dots & 0 \\ 0 & c_3^{3,n} & \dots & 0 \\ \vdots & \vdots & \ddots & \vdots \\ 0 & 0 & \dots & a_2^n c_3^{M-1,n} - a_3^n c_2^{M-1,n} \end{pmatrix}, \quad (11)$$

$$\mathbf{B}_n = \begin{pmatrix} 1 + \beta_n c_1^{2,n} & c_2^{2,n} & 0 & \dots & 0 \\ c_1^{3,n} & 1 & c_2^{3,n} & \dots & 0 \\ \vdots & \vdots & \vdots & \ddots & \vdots \\ 0 & 0 & \dots & a_2^n c_1^{M-1,n} - a_1^n c_2^{M-1,n} & a_2^n - c_2^{M-1,n} \end{pmatrix}, \quad (12)$$

$$\mathbf{C}_n = \begin{pmatrix} c_4^{2,n} & 0 & \dots & 0 \\ 0 & c_4^{3,n} & \dots & 0 \\ \vdots & \vdots & \ddots & \vdots \\ 0 & 0 & \dots & a_2^n c_4^{M-1,n} - a_3^n c_4^{M-1,n} \end{pmatrix}, \quad (13)$$

and \mathbf{F}^n is the excitation column vector given by

$$\mathbf{F}^n = \begin{pmatrix} -c_1^{2,n}(\beta_n \chi_1^n - \chi_0^n) \\ 0 \\ \vdots \\ 0 \end{pmatrix}. \quad (14)$$

In the above matrices, $c_k^{m,n}$ is the k th finite difference coefficient associated with the node at (x_m^n, y_m^n) , and a_k^n is the k th MEI coefficient associated with the node at (x_M^n, y_M^n) . The system of equations defined by (8-10) can be solved efficiently by the Ricatti block-by-block elimination technique [8] described in II e. After the scattered field is solved in the

interior domain, the total field on the scatterer can be recovered from (6). The field at any point can then be determined from the total field on the scatterer by using the integral representation given in the next section. In the next few sections, we give details of the various steps presented in this section.

IIb. Integral Representation:

Fig. 1. shows an electric line source \vec{J}_0 located at $O(x_o, y_o)$. It is required to find the total field (\vec{E}, \vec{H}) , at an arbitrary point $P(x_p, y_p)$ over the irregular, inhomogeneous terrain. We will employ the reciprocity theorem [2] to express the total field in terms of the scattered field and an incident field, (\vec{E}_0, \vec{H}_0) , defined to exist over a flat, constant impedance plane, C_0 , of normalized impedance Δ_o . The general relationship between a surface impedance Δ and the local ground constants $(\epsilon_o \epsilon_r, \mu_o, \sigma)$ is

$$\Delta = 1/\sqrt{(\epsilon_r - j\sigma_r)}, \quad (15)$$

where σ_r is the relative conductivity representing $\sigma/\omega\epsilon_o$, σ being the actual conductivity of earth. The above relationship is used to evaluate not only Δ_o , but also Δ_s that will be encountered below. The field (\vec{E}, \vec{H}) is different from (\vec{E}_0, \vec{H}_0) due to (a) the terrain inhomogeneities, or (b) terrain irregularities, or (c) both. Let (\vec{E}_1, \vec{H}_1) be the fields due to sources (\vec{J}_1, \vec{M}_1) located at $P(x_p, y_p)$ over the reference impedance plane. The fields '0' and '1' satisfy the impedance boundary condition $\hat{y} \times \vec{E}_1 = \eta_o \Delta_o \hat{y} \times (\hat{y} \times \vec{H}_1)$ on C_0 , where \hat{y} is the unit normal on C_0 . The total fields satisfy the impedance boundary condition $\hat{y} \times \vec{E} = \eta_o \Delta_s \hat{n} \times (\hat{n} \times \vec{H})$ on the terrain surface C , where the impedance Δ_s is possibly different from Δ_o , and may vary from point to point. The surface C is assumed to consist of flat portions C_f where the impedance Δ_s deviates from Δ_o and/or C_t where the terrain deviates from being flat. The remaining portion C_r of the surface is coincident with the corresponding portions of C_0 . The surface C_b is the projection of C_t onto C_0 . Let C_∞ be a semicircular cylinder bounded at infinity, and A be the interior region bounded by the surfaces C and C_∞ . The unit normal \hat{n} points into the region A . It is assumed that the ground deviates from the reference plane only in the positive y direction. Thus, we consider only hilly obstacles and do not address the problem of trenches in a flat plane. The ground constants are, however, allowed to have variations along the terrain.

The fields $(\vec{E} - \vec{E}_0, \vec{H} - \vec{H}_0)$ have no sources in the region A , and satisfy source-free Maxwell's equations, while the fields (\vec{E}_1, \vec{H}_1) satisfy Maxwell's equations with sources (\vec{J}_1, \vec{M}_1) . From a two dimensional version of the reciprocity theorem [2], we have

$$\int_{C_r+C_f+C_t+C_\infty} [(\vec{E} - \vec{E}_0) \times \vec{H}_1 - \vec{E}_1 \times (\vec{H} - \vec{H}_0)] \cdot \hat{n} d\ell = \iint_A [(\vec{E} - \vec{E}_0) \cdot \vec{J}_1 - (\vec{H} - \vec{H}_0) \cdot \vec{M}_1] da \quad (16)$$

The contour integral over C_∞ vanishes due to the Sommerfeld radiation conditions [11]. Since (\vec{E}, \vec{H}) and (\vec{E}_0, \vec{H}_0) satisfy the same boundary conditions on C_r , the integral over it vanishes. Applying reciprocity theorem to the source-free region bounded by $C_t - C_b$, we obtain

$$\int_{C_t-C_b} [\vec{E}_0 \times \vec{H}_1 - \vec{E}_1 \times \vec{H}_0] \cdot \hat{n} d\ell = 0, \quad (17)$$

Hence

$$\int_{C_t} [\vec{E}_0 \times \vec{H}_1 - \vec{E}_1 \times \vec{H}_0] \cdot \hat{n} d\ell = \int_{C_b} [\vec{E}_0 \times \vec{H}_1 - \vec{E}_1 \times \vec{H}_0] \cdot \hat{n} d\ell = 0. \quad (18)$$

The last equality follows from the fact that the '0' and '1' fields satisfy the same impedance boundary conditions on C_b . Making use of these in (16) we get

$$\iint_A [(\vec{E} - \vec{E}_0) \cdot \vec{J}_1 - (\vec{H} - \vec{H}_0) \cdot \vec{M}_1] da = \int_{C_f+C_t} (\vec{E} \times \vec{H}_1 - \vec{E}_1 \times \vec{H}) \cdot \hat{n} d\ell. \quad (19)$$

Next, we pick a \hat{z} -directed magnetic line source of unit voltage for \vec{M}_1 and choose $\vec{J}_1 = 0$ to arrive at

$$\hat{z} \cdot \vec{H}(P) = \hat{z} \cdot \vec{H}_0(P) - \int_{C_f+C_t} [(\hat{n} \times \vec{E}) \cdot \vec{H}_1^{(z)} + (\hat{n} \times \vec{H}) \cdot \vec{E}_1^{(z)}] d\ell, \quad (20)$$

where $(\vec{E}_1^{(z)}, \vec{H}_1^{(z)})$ is the field due to a \hat{z} -directed magnetic line source of unit voltage located at the field point P . We relate $(\hat{n} \times \vec{H})$ and $(\hat{n} \times \vec{E})$ on $C_f + C_t$ by means of the impedance boundary condition to finally obtain

$$\hat{z} \cdot \vec{H}(P) = \hat{z} \cdot \vec{H}_0(P) - \int_{C_f+C_t} [\vec{E}_1^{(z)}(Q) - \eta_o \Delta_s (\hat{n} \times \vec{H}_1^{(z)}(Q))] \cdot (\hat{n} \times \vec{H}(Q)) d\ell_Q. \quad (21)$$

The above equation is rewritten as

$$H_z(P) = H_{0z}(P) - \int_{C=C_f+C_i} H_z(Q) \mathcal{G}(Q,P) d\ell_Q, \quad (22)$$

where

$$\mathcal{G}(Q,P) = E_{1\ell}^{(z)}(Q) - \eta_o \Delta_s H_{1z}^{(z)}(Q) \quad (23)$$

is defined as the Green's function at Q due to a z -directed magnetic line source located at P over a plane of impedance Δ_o . The unit tangent $\hat{\ell}$ to the contour is defined such that $\hat{\ell} \times \hat{n} = \hat{z}$. Equation (22) may be used to set up an integral equation for the unknown H_z and solved numerically. However this will be computationally intensive as already discussed and will not be considered in the present report. In the next section, we present expressions for H_{0z} and $\mathcal{G}(Q,P)$ which allow rapid numerical computation.

IIc. Incident Magnetic Field and Green's Function:

Fig. 4. shows a transversely polarized electric line source located at (x_o, y_o) over a plane of constant impedance Δ_o . Due to the impedance boundary condition we have $E_{0x} = \eta_o \Delta_o H_{0z}$. The line source carries a total current I_o and has its current moment directed along the unit vector \hat{i} which makes an angle θ_o with the x -axis. The current moment corresponding to the mirror image of the source about a perfectly conducting plane at $y = 0$ points in a direction \hat{i}' which makes an angle $\pi - \theta_o$ with the x -axis. The current density of the line source is expressed as

$$\vec{J} = \hat{i} I_o k_o^2 \delta(x - x_o) \delta(y - y_o) \stackrel{\text{def}}{=} k_o^2 \vec{I}, \quad (24)$$

where $\delta(\cdot)$ represents a unit delta function. The magnetic vector potential $\vec{A} = \hat{x} A_x + \hat{y} A_y$ satisfies

$$\nabla^2 \vec{A} + \vec{A} = -\mu_o \vec{I}. \quad (25)$$

It is easily seen from Maxwell's equations that

$$H_{0z} = \frac{\omega}{\eta_o} \left[\frac{\partial A_y}{\partial x} - \frac{\partial A_x}{\partial y} \right] \quad (26)$$

$$E_{0x} = -j\eta_o \frac{\partial H_{0z}}{\partial y}. \quad (27)$$

Equation (25) can be separated into its respective cartesian components. A vertical current excites a vertical component, A_y , of the vector potential, whereas, a horizontal component excites only a horizontal component, A_x . It is to be noted here that a horizontally polarized *line source* will only need A_x for the satisfaction of the boundary conditions at $y = 0$. This is in contrast to the three-dimensional case where a HED requires both A_x and A_z for the satisfaction of boundary conditions. We take a Fourier transform on both sides of (25) with respect to the x -axis, and denote the transformed quantities with a tilde and the normalized transform variable by k_x . When this is done, an inhomogeneous harmonic equation with respect to y is obtained in the transformed domain. The components of the vector potential can be determined from it as

$$\tilde{A}_x(k_x, y; x_o, y_o) = \frac{\mu_0 I_0 \cos \theta_0 e^{jk_x x_o}}{4\pi j \beta} \left\{ e^{-j\beta|y-y_o|} + R_h(\beta) e^{-j\beta(y+y_o)} \right\} \quad (28)$$

$$\tilde{A}_y(k_x, y; x_o, y_o) = \frac{\mu_0 I_0 \sin \theta_0 e^{jk_x x_o}}{4\pi j \beta} \left\{ e^{-j\beta|y-y_o|} + R_v(\beta) e^{-j\beta(y+y_o)} \right\}, \quad (29)$$

where $R_h(\beta)$ and $R_v(\beta)$ are the reflection coefficients for the horizontal and vertical polarizations respectively, and $k_x^2 + \beta^2 = 1$. Imposition of the impedance boundary condition at $y = 0$ yields

$$R_v(\beta) = -R_h(\beta) = 1 - \frac{2\Delta_o}{\beta + \Delta_o}. \quad (30)$$

The components of vector potential in the space domain are obtained by taking the inverse Fourier transformation of (28) and (29). Letting the free-space Green's function Π as

$$\Pi(x, y; x_o, y_o) = \int_{-\infty}^{\infty} \frac{e^{-j[k_x(x-x_o) + \beta|y-y_o|]}}{\pi \beta} dk_x = H_0^{(2)}[\sqrt{(x-x_o)^2 + (y-y_o)^2}], \quad (31)$$

we arrive at

$$\vec{A} = \frac{\mu_0 I_0}{4j} \left\{ \hat{i} \Pi(x, y; x_o, y_o) + \hat{i}' [\Pi(x, y; x_o, -y_o) - 2\Delta_o \delta \Pi(x, y; x_o, y_o)] \right\}, \quad (32)$$

where

$$\delta \Pi(x, y; x_o, y_o) = \int_{-\infty}^{\infty} \frac{e^{-j[\beta(y+y_o) + k_x(x-x_o)]}}{\pi \beta (\beta + \Delta_o)} dk_x. \quad (33)$$

The integral defined in (33) is of the so called Sommerfeld type and difficult to evaluate directly. To efficiently compute the incident magnetic field and the Green's function, we

will incorporate the ideas contained in [12] and [13]. For small distances, we use a modified method of [13]. For large horizontal distances, where the method of [13] fails, we have used a modified version of the method in [12].

For small distances, we employ the clever device originally used by Chow, *et al.*, [13] to calculate the Green's function for microstrip structures. The key to the procedure is to convert (31) to an integral over the complex β -plane and make approximations to (33). Firstly, we note that the imaginary part of β must be chosen appropriately (i.e., $\Im(\beta) < 0$) such that integral in (31) converges for all $|y - y_o| > 0$. By a change of variable, (31) may be converted to an integral in terms of β as

$$H_0^{(2)}[\sqrt{(x - x_o)^2 + (y - y_o)^2}] = \frac{2}{\pi} \int_{\Gamma_1} \frac{e^{-j\beta|y-y_o|}}{k_x} \cos[k_x(x - x_o)] d\beta, \quad (34)$$

where the contour of integration, Γ_1 , is shown in Fig. 5. Similarly,

$$\delta\Pi(x, y; x_o, y_o) = \frac{2}{\pi} \int_{\Gamma_1} \frac{e^{-j\beta(y+y_o)}}{k_x(\beta + \Delta_o)} \cos[k_x(x - x_o)] d\beta. \quad (35)$$

The contour of integration for $\delta\Pi$ may be deformed to a modified contour, Γ_2 , since no singularities are enclosed between it and Γ_1 (see Fig. 5). The contour Γ_2 consists of two parts: a straight line, Γ_s , drawn from $(1, 0)$ to $(0, -jT_0)$, for some chosen positive constant T_0 , and a portion coincident with that of Γ_1 . Most of the contribution to the integral comes from the former as the integrand decays exponentially on the latter for sufficiently large $y + y_o$. The trick is to approximate the spectral function $1/(\beta + \Delta_o)$ over Γ_s as a finite *sum* of complex exponentials of the form

$$\frac{1}{(\beta + \Delta_o)} \approx \sum_{k=1}^{N_T} A_k e^{-t_k \beta}. \quad (36)$$

The complex constants A_k and t_k can be determined by the Prony's method [14]. Substituting this into (35) we have

$$\delta\Pi(x, y; x_o, y_o) \approx \sum_{k=1}^{N_T} A_k \frac{2}{\pi} \int_{\Gamma_2} \frac{e^{-j\beta(y+y_o-jt_k)}}{k_x} \cos[k_x(x - x_o)] d\beta$$

$$\begin{aligned}
& + \frac{2}{\pi} \int_{\beta=-jT_0}^{-j\infty} \frac{e^{-j\beta(y+y_o)} \cos[k_x(x-x_o)]}{k_x} \left[\frac{1}{(\beta + \Delta_o)} - \sum_{k=1}^{N_T} A_k e^{-t_k \beta} \right] d\beta \\
& = \sum_{k=1}^{N_T} A_k H_0^{(2)}(R_k) + \frac{2}{\pi T_0} \Re [z_2 E_1(z_2) - e^{-z_2}] \\
& - \frac{j}{\pi} \sum_{k=1}^{N_T} A_k [E_1(z_2 - jt_k T_0) + E_1(z_2^* - jt_k T_0)]. \tag{37}
\end{aligned}$$

The first term of the last equality follows by comparison with (34). The quantity R_k is the distance between the observation point (x, y) and the complex image at $(x_o, -y_o + jt_k)$ given by $R_k = \sqrt{(x - x_o)^2 + (y + y_o - jt_k)^2}$, with the square root chosen such that $\Re(R_k) > 0$, and $z_2 = [(y + y_o) + j(x - x_o)]T_0$. The remaining integral in (37) over the negative imaginary axis has been performed in closed form in terms of exponential integrals, $E_1(\cdot)$ [21], by using the approximations $\beta + \Delta_o \approx \beta$ and $k_x \approx -j\beta$. The quantity $\delta\Pi$ can be calculated much faster using (37) rather than (33) or (35). However, when $y + y_o$ is small and $|x - x_o|$ is large, the contribution arising from the tail of Γ_2 becomes important, and the exponential approximation to the spectral function in (36) requires many terms. Using only a few terms leads to large errors in the computation of $\delta\Pi$. The accuracy can be greatly improved at the cost of computational time by expressing the spectral function $1/(\beta + \Delta_o)$ over Γ_s as a Laplace *integral* of the form

$$\frac{1}{(\beta + \Delta_o)} = \int_{t=0}^{\infty} e^{-\Delta_o t} e^{-\beta t} dt. \tag{38}$$

Such a procedure was suggested in [12]. The Laplace transform of the spectral function in (38) converges for $-\pi/2 - \arg(\Delta_o) < \arg(t) < \pi/2 - \arg(\Delta_o)$. Substituting this into (35) and changing the order of integration, we arrive at

$$\delta\Pi(x, y; x_o, y_o) = \int_{t=0}^{\infty} e^{-\Delta_o t} H_0^{(2)}(D) dt, \tag{39}$$

with the complex distance $D = \sqrt{(x - x_o)^2 + (y + y_o - jt)^2}$ defined such that $\Re(D) > 0$ for representing an outgoing wave and $\Im(D) < 0$ for the convergence of the integral. Even though it is much faster to compute $\delta\Pi$ using (39) than using (35), the integration can be

slow for certain combinations of Δ_o , $(x - x_o)$, and $(y + y_o)$. This is because the integrand decays rather slowly on the positive real axis of the t -plane. To further aid fast evaluation of the integral (39), we deform the original contour in the complex t -plane to one over which the asymptotic form of the Hankel function decays most rapidly (steepest descent path). This is obtained by setting $\Re[D(t)] = \Re[D(t = 0)] = r_2$ on the deformed contour, where $r_2 = \sqrt{(x - x_o)^2 + (y + y_o)^2}$ is the distance of the observation point from the mirror image. If $t = u + jv$, the steepest descent path through $t = 0$ can be obtained as

$$u \longrightarrow [0, \infty), \quad v = -(y + y_o) + r_2 \sqrt{\frac{u^2 + (y + y_o)^2}{u^2 + r_2^2}} \quad (40)$$

on which the distance function is

$$D = r_2 - ju \sqrt{\frac{u^2 + (y + y_o)^2}{u^2 + r_2^2}}. \quad (41)$$

Evaluation of the integral over the steepest descent path permits rapid computation of $\delta\Pi$. Although this is true uniformly for all $x - x_o$ and $y + y_o$, it is less efficient than (37) for small values of r_2 . This is due to the presence of the Hankel function with complex arguments in the integrand of (39), which, one has to evaluate repeatedly to perform the integration. Hankel functions need be computed only for a fixed number of arguments in (37) in contrast to the several tens of times needed when (39) is used. It is very important indeed to reduce the time required to compute the incident field and the Green's function, particularly when one has to evaluate them several thousands of times as in the present method. This point will be appreciated shortly when we discuss the MEI method.

Combining (26) and (32) the incident magnetic field can be obtained as

$$H_{0z} = \frac{-k_0 I_o}{4j} \left\{ \sin(\theta_0 - \theta_1) H_1^{(2)}(r_1) + \sin(\theta_0 + \theta_2) H_1^{(2)}(r_2) \right. \\ \left. + 2\Delta_o \left(\sin \theta_0 \frac{\partial}{\partial x} + \cos \theta_0 \frac{\partial}{\partial y} \right) \delta\Pi(x, y; x_o, y_o) \right\}, \quad (42)$$

where $r_1 = \sqrt{(x - x_o)^2 + (y - y_o)^2}$, and $\theta_1(\theta_2)$ is the positive angle made with the x -axis by the straight line joining the observation point and the source (mirror image) point.

Using a similar analysis, the Green's function (defined through (23)) at the point $Q(x_q, y_q)$ due to a unit voltage, z -directed, magnetic line source located at $P(x_p, y_p)$ can

be obtained as

$$\mathcal{G}(Q,P) = \frac{-1}{4j} \left\{ \sin(\theta - \theta_3) H_1^{(2)}(r_3) + \sin(\theta - \theta_4) H_1^{(2)}(r_4) - j\Delta_s \left[H_0^{(2)}(r_3) + H_0^{(2)}(r_4) \right] \right. \\ \left. + 2\Delta_o \left[j\Delta_s + \sin\theta \frac{\partial}{\partial x_q} - \cos\theta \frac{\partial}{\partial y_q} \right] \delta\Pi(x_q, y_q; x_p, y_p) \right\}, \quad (43)$$

where $r_3 = \sqrt{(x_q - x_p)^2 + (y_q - y_p)^2}$, $r_4 = \sqrt{(x_q - x_p)^2 + (y_q + y_p)^2}$, $\theta_3(\theta_4)$ is the positive angle made with the x -axis by the straight line joining the observation point Q and the source point P (mirror image), and θ is the angle made with the positive x -axis by the unit tangent at Q .

An integral equation may be derived for the unknown, H_z , on the scatterer by substituting the above Green's function into (22) and taking the limit as the point P approaches the scattering boundary from outside. When this is done, one gets

$$H_z(P) = 2H_{0z}(P) - 2 \int_{C=C_f+C_t} H_z(Q) \mathcal{G}(Q,P) d\ell_Q, \quad P, Q \in C_f + C_t, \quad (22')$$

where the integral is understood to be of Cauchy's principal value type. The first term on the right can be regarded as the physical optics approximation to the surface field in the illuminated region.

The far-zone ($r \rightarrow \infty$) fields can be determined by using the principal asymptotic forms for the various Hankel functions. For the quantity $\delta\Pi$, far-zone approximation can be obtained by deforming the path of the integral in (33) and evaluating by the saddle point method. The result is

$$\delta\Pi(x, y; x_o, y_o) \sim \sqrt{\frac{2j}{\pi r_2}} \frac{e^{-jr_2}}{(\Delta_o + \sin\theta_2)}. \quad (44)$$

Having provided the integral representation and expressions for the various fields, we present in the next section details on the MEI method of terminating the computational domain in the finite scheme.

II.d. *MEI Method:*

As already remarked, the MEI method allows one to generate near-field conditions for the scattered field ψ to simulate free space at the terminating boundary. We will describe

the procedure to determine the coefficients a_k in (7). Mei *et al.*, [4] postulated that there exists a linear combination of the scattered field over a small, discrete, spatial domain, $\vec{\rho}_k$, such that

$$\psi_0 + \sum_{k=1}^K a_k \psi_k = 0. \quad (45)$$

The coefficients a_k are postulated to be dependent upon the location of the field and geometry of the scatterer, but, independent of the excitation of the scattered field. The last postulate enables one to determine the coefficients a_k using a finite set of linearly independent scattered fields caused by different excitations. It is not the purpose of the present report to test the validity of these postulates. Rather, we employ this method to develop a relatively fast numerical method for predicting both the sky wave as well as the ground wave for propagation over inhomogeneous and irregular terrain. The starting point is an accurate representation of near fields such as equation (22). The scattered field is given from (22) as

$$\psi(\vec{\rho}) = H_z(\vec{\rho}) - H_{0z}(\vec{\rho}) = - \int_C H_z(\vec{\rho}') \mathcal{G}(\vec{\rho}', \vec{\rho}) d\ell'. \quad (46)$$

Making use of this in (45) we see that

$$\int_C H_z(\vec{\rho}') \left[\mathcal{G}(\vec{\rho}', \vec{\rho}_0) + \sum_{k=1}^K a_k \mathcal{G}(\vec{\rho}', \vec{\rho}_k) \right] d\ell' = 0. \quad (47)$$

The specific excitations (which they termed as *metrons*) suggested by Mei *et al.*, were

$$H_z = 1, \cos(2\pi s), \sin(2\pi s), \cos(4\pi s), \text{ and } \sin(4\pi s), \quad (48)$$

where s is the normalized arc length that varies between 0 and 1 on the scatterer. We will label these as *sinusoidal metrons*. We were not able to consistently generate meaningful results using sinusoidal metrons, and thus considered other choices. A closer look at (47) provides insight as to why the sinusoidal metrons cannot be expected to work all the time. Since the coefficients a_k have been postulated to be independent of the excitation (which determines $H_z(\vec{\rho}')$ on the scatterer), it is implied that the terms within the bracket be identically zero for all points $\vec{\rho}'$ on the scatterer. The term $\mathcal{G}(\vec{\rho}', \vec{\rho}_k)$ is the field at $\vec{\rho}'$ due

to a line source located at $\vec{\rho}_k$. Hence we require that the field due to a linear combination of these line sources ($K + 1$ in number) vanish *pointwise* on the scatterer. But this would be difficult to accomplish as there are only a *few* discrete sources (K is typically 4–5 depending on the type of the computational molecule chosen). This is particularly true for a large scatterer. A more reasonable criterion is to require that the field be minimum in some sense on the scatterer. We choose the coefficients a_k so that integrated square residual

$$R = \int_C \left| \mathcal{G}(\vec{\rho}', \vec{\rho}_0) + \sum_{k=1}^K a_k \mathcal{G}(\vec{\rho}', \vec{\rho}_k) \right|^2 d\ell' \quad (49)$$

is a minimum on the scatterer. In other words, we determine the coefficients by requiring that $\frac{\partial R}{\partial a_k} = 0$. This position was first taken by Jetvic and Lee [16], who considered the case of perfectly conducting cylinder to demonstrate the success of this approach. This criterion results in

$$\sum_{k=1}^K a_k \int_C \mathcal{G}(\vec{\rho}', \vec{\rho}_k) \mathcal{G}^*(\vec{\rho}', \vec{\rho}_n) d\ell' = - \int_C \mathcal{G}(\vec{\rho}', \vec{\rho}_0) \mathcal{G}^*(\vec{\rho}', \vec{\rho}_n) d\ell', \quad n = 1, 2, \dots, K. \quad (50)$$

The coefficients a_k can be obtained by solving the linear system defined by (50). We shall label the particular choice of metrons in (50) as the \mathcal{G}^* *metrons*. The coefficient matrix in (50) is Hermitian symmetric. The number of integrals required per a five-point star mesh ($K = 4$) is 14. If every node is utilized in the evaluation of an integral, the total number of flops required to perform the integration per a five star mesh is $14N$. The number of Green's function evaluations per a five-point star mesh is $5N$. The total time required to fill the coefficient matrix in (50) for N nodes on the object boundary is then $14N^2 t_f + 5N^2 t_g = O(N^2)$, where t_f and t_g are the respective times required per flop and a single evaluation of the Green's function. For example, if it takes 1 millisecond for a single evaluation of the Green's function, the total time spent in the evaluation of the Green's functions for $N = 1000$ would be 83 minutes. It is therefore very important to minimize the time required to calculate the Green's function. The total time needed to fill the matrices (11) through (14) is still of order $O(N^2)$. The fill time may be reduced approximately by a factor of half by skipping every other point in the evaluation of the integrals. The next section deals with the inversion of the block system defined in (8–10).

He. Inversion by Ricatti Transform

The overall matrix generated by the block system of equations in (8–10) is highly sparse and is almost tridiagonal. It may be inverted efficiently by the Ricatti transform method [8], which was originally described in [17]. To this end we write

$$\Psi^{n-1} = \mathbf{R}_n \Psi^n + \mathbf{S}_n, \quad n = 2, \dots, N, \quad (51)$$

where the transform matrix \mathbf{R}_n is of order $M \times M$, and the shift vector \mathbf{S}_n is of order $M \times 1$. Substituting into equation (9), we get

$$\Psi^n = -[\mathbf{A}_n \mathbf{R}_n + \mathbf{B}_n]^{-1} \mathbf{C}_n \Psi^{n+1} + [\mathbf{A}_n \mathbf{R}_n + \mathbf{B}_n]^{-1} [\mathbf{F}^n - \mathbf{A}_n \mathbf{S}_n]. \quad (52)$$

We then observe by comparing with (51) that for $n = 2, \dots, N - 1$

$$\mathbf{R}_{n+1} = -[\mathbf{A}_n \mathbf{R}_n + \mathbf{B}_n]^{-1} \mathbf{C}_n, \quad \mathbf{S}_{n+1} = [\mathbf{A}_n \mathbf{R}_n + \mathbf{B}_n]^{-1} [\mathbf{F}^n - \mathbf{A}_n \mathbf{S}_n]. \quad (53)$$

The end equation (8) may be used to determine the transform matrix \mathbf{R}_2 and \mathbf{S}_2 . Substituting (51) into (8) and carrying out some algebraic manipulations, we get

$$\mathbf{R}_2 = (\mathbf{A}_1 \mathbf{C}_2^{-1} \mathbf{A}_2 - \mathbf{B}_1)^{-1} (\mathbf{C}_1 - \mathbf{A}_1 \mathbf{C}_2^{-1} \mathbf{B}_2), \quad (54)$$

and

$$\mathbf{S}_2 = (\mathbf{A}_2 - \mathbf{C}_2 \mathbf{A}_1^{-1} \mathbf{B}_1)^{-1} (\mathbf{F}^2 - \mathbf{C}_2 \mathbf{A}_1^{-1} \mathbf{F}^1). \quad (55)$$

The higher order matrices can be determined from the above two by using the recursive relations in (53). Finally, by using the other end equation (10) in conjunction with (51), we solve for Ψ^N as

$$\Psi^N = [(\mathbf{A}_N + \mathbf{C}_N \mathbf{R}_{N-1}) \mathbf{R}_N + \mathbf{B}_N]^{-1} [\mathbf{F}^N - \mathbf{C}_N \mathbf{S}_{N-1} - (\mathbf{A}_N + \mathbf{C}_N \mathbf{R}_{N-1}) \mathbf{S}_N]. \quad (56)$$

The remaining vectors $\Psi^{N-1}, \Psi^{N-2}, \dots, \Psi^1$ can then be determined by the tranformation equations in (51). Each of the matrices \mathbf{A}_n , \mathbf{C}_n , \mathbf{S}_n , and Ψ^n has M non-zero elements while \mathbf{B}_n has $3M$ non-zero elements. The matrix \mathbf{R}_n is dense and has M^2 elements. The total number of non-zero elements, N_s , that need to be stored with this algorithm is then

$$N_s = (N - 1)(M^2 + M) + 6MN \simeq (M + 7)MN = O(N). \quad (57)$$

For example, with $N = 1000$ and $M = 5$, the algorithm needs around 0.96 MB of RAM for implementation in double precision. If N is now increased to 10,000, the required memory is increased to 9.6 MB. This is in contrast to the integral equation methods, where, a scaling in N by a factor of 10 results in 100 fold increase in memory. The inversion time of the algorithm is only of order $O(N)$. The overall CPU time of the present method is dominated by the matrix fill time discussed in the previous section.

III. NUMERICAL RESULTS

The entire code was developed in double precision in FORTRAN. The linear equations generated by (4) and (5) for the determination of the coefficients c_k were solved by Gaussian elimination. Due to the generation of a highly ill-conditioned matrix, Gaussian elimination is, however, not reliable for the inversion of the matrix associated with the coefficients a_k . By treating it as a linear least square problem, we have used Singular Value Decomposition (SVD) [19] to construct a minimum norm solution to the matrix equation. SVD is also appropriate for the case of sinusoidal metrons where we generate more equations than the number of unknowns. The effective rank of the matrix is determined by treating as zero those singular values which are less than a predetermined number 'Rcond' times the largest singular value. The condition number, κ_2 , of the matrix in the 2-norm is the ratio of the highest singular value to the lowest singular value. Of course, if Rcond is set less than the infimum of $1/\kappa_2$ over all the nodes on the boundary, SVD uses all the singular vectors and produces the same result as Gaussian elimination for a square matrix. Integration in (46) was performed by the Simpson's rule either using all nodes on the scatterer or using every other node. The latter reduces the integration time by a factor of half. The geometry of the scatterer was specified in a discrete form by the nodes at which the unknowns are defined. Interpolation with quadratic elements [20] was used to generate a continuous object. In this way the code was capable of handling a rather arbitrary geometry. The various Hankel functions with complex arguments in (37) and (39) were generated by implementing the algorithm of du Toit [15].

To verify calculations by the complex image approach of section IIc, we first present results on the computation of the incident magnetic field. Fig. 6 shows the magnitude of the normalized magnetic field due to a vertically polarized line source on the surface of a flat, lossy plane. The ground constants correspond to $\epsilon_r = 15$ and $\sigma_r = 6$. The magnetic field is normalized to the free-space value, which is true of all the results shown in the report. The constant T_0 was chosen to be at least 5 to make the approximation in (37) valid. Fourteen complex images were chosen to approximate the spectral function, although 10 were found to produce identical results. Expression (37) was used for $r_2 < 50$, while (39) was used otherwise. The upper limit for u on the steepest descent path in the integral

(39) is determined such that the imaginary part of the complex distance D takes a value of 5. The arc length value in Fig. 6 is equal to zero right under the source. Comparison is shown with the calculation based on Sommerfeld integral given in [1]. Excellent agreement is seen between the two, thus validating the complex image approach. Several other cases have also been successfully tested including the cases of large conductivity such as $\epsilon_r = 10$, and $\sigma_r = 200$. Where applicable, we used $N_T = 10$ and $T_0 = 5$ in the numerical results shown in this report.

We next compare the numerical results for propagation over a semicircular boss on a perfectly conducting plane ($\Delta_o = 0$), for which the exact solution in terms of cylindrical harmonics exists [1]. Results are shown both for the sinusoidal metrons and the G^* metrons. A vertically polarized source ($\theta_0 = 90$) was assumed to be located at $(-0.75\lambda, 0.1\lambda)$ near a semicircular boss of radius 0.5λ with center at the origin. Six layers ($M = 4$, recalling that M denotes the number of *interior* layers not counting the object and outer boundaries) with an inter-layer spacing, h , of 0.05λ were used to discretize the computational domain. The distance between the outermost layer and the object boundary is $(M+1)h = 0.25\lambda$. The outer boundary was discretized into roughly twenty segments per wavelength resulting in $N = 49$. Rcond for SVD was set at 1.D-6. The arc length, S , takes a value 0 at the left end of the boss and increases in the clockwise direction. Fig. 7 shows a good agreement for the magnitude of the surface magnetic fields between the numerical and the exact results both for the sinusoidal and G^* metrons. The supremum, Ω (indicated as 'Con' in the plots), of the 2-norm condition number of the 4×4 coefficient matrix in the case of G^* metrons, and the 5×4 matrix in the case of sinusoidal metrons over all nodes on the boundary is also indicated on the plot. Fig. 8 shows a comparison of the relative pattern of the source in the presence of the boss. Good agreement is seen except near the grazing angles in the shadow region where a discrepancy of about 2 dB is seen. The accuracy of the solution can be affected by varying Rcond, M , N and h . While it is generally true that the accuracy improves when M or N is increased or when h is decreased, difficulty to compute the various quantities precisely over a small, discrete, spatial domain tends to obscure this. The last two parameters affect the discretization errors, while M and h together influence the distance between the object boundary and

the outer boundary. All other parameters being fixed, if M is increased and h is decreased while maintaining a constant separation between the object and outer boundaries, the solution improves only slightly as indicated in Figs. 9 and 10. In Fig. 9 we use $M = 6$ and $h = 0.0357\lambda$, while in Fig. 10 we use $M = 8$ and $h = 0.0278\lambda$. The slight improvement over the results of Fig. 7 is thought to be due to a decreased discretization error achieved by the use of smaller h . Compared to Fig. 7 it is also seen that Ω increases in both cases. This is due to the larger size of the matrices involved. The effect of integration on the numerical solution was also investigated. In one case, integration was performed by using all nodes on the boundary, while in the other case every other node was used. The former is labeled as full integration, while the latter as half integration. Fig. 11 shows the results with full and half integration. The solution is less sensitive to integration for the G^* case than it is for the sinusoidal metron case. This trend has been noticed for other shapes as well. To see the effect of node density on the solution, the number of segments on the outer boundary was increased to 29 per wavelength. This was with a view to increase the accuracy of the solution. Fig. 12 shows the solution with the higher node density. The G^* metron solution appears to have improved slightly, whereas the sinusoidal metron case deteriorated slightly when compared with the 20 segment/wavelength case of Fig. 9. Note the increase Ω for both cases when compared to Fig. 9. This is because the fields calculated over a small spatial domain tend to be more linearly dependent than over a larger domain.

Parametric studies were also made for larger cylinders. Fig. 13 shows the results for a radius of 5λ . With the indicated choice of parameters, the number of nodes on the boundary is $N = 331$. Once again the agreement between numerical and exact results is good. Some spurious oscillations are, however, seen in the numerical solution in the last part of the shadow region. The total computational time needed on a 80486-50 Personal Computer for the calculation of ground wave data at 331 points and the far-zone data at 181 angles utilizing every other point for integration was $2\frac{1}{2}$ minutes. Almost all of the time was required for filling the various matrices, with the inversion taking only a paltry 1 second. Fig. 14 shows the relative pattern of the source. It is seen that a slightly better agreement is obtained with the sinusoidal metrons than with the G^* metrons. As in the

previous case the accuracy improved only slightly when the number of interior layers is increased without changing the distance between the object and outer boundaries. This is clearly seen from Figs. 15 and 16 which show results for $M = 6$ and $M = 8$ respectively. For the sinusoidal case, however, the result with $M = 8$ is once again less accurate when compared with $M = 4$. Increasing R_{cond} had no effect on the solution. However, when the number of segments on the outer boundary is increased to 34 per wavelength, a more accurate solution is obtained as seen in Fig. 17. At this node density the spacing between nodes on the object boundary is the same as h . Fig. 18 shows the numerical solution with the higher node density of 34 segments per wavelength for $M = 8$ and $h = 0.0278\lambda$. For the G^* metron case the solution remains practically unchanged from that of Fig. 16, but the result for sinusoidal metron case is more meaningful with the higher node density. The effect of moving the terminating boundary further away from the object boundary is seen by examining Fig. 19. For the parameters indicated, the outer boundary is at a distance of 0.45λ from the cylinder. For the G^* metron case, the hump in the solution around $S = 70$ is still present, although an improvement is seen at the left end of the boss (the illuminated side). Overall, the G^* solution agrees better with the exact solution when compared with Fig. 13 where the separation between the boundaries is 0.25λ . Increasing the node density to 34 per wavelength did not improve the solution any further. Further improvement in the solution can be affected by decreasing h which decreases the discretization errors. This is clearly seen from Fig. 20 where the solution with $h = 0.035\lambda$ compares better than the one with $h = 0.05\lambda$. The spurious oscillations can be reduced by (i) increasing the separation between the object and the terminating boundaries, and (ii) concurrently discarding those singular vectors that are corrupted by roundoff errors. The latter is accomplished by decreasing R_{cond} during the SVD solution of the coefficients a_k . In general, it has been found that for a given spatial resolution, the coefficient matrix becomes more ill-conditioned (as evidenced by a higher condition number) as the separation between the object and outer boundaries gets larger. Consequently, R_{cond} has to be set a lower value in order to achieve a meaningful solution. Fig. 21 shows the solution for a separation of 0.6λ and $R_{\text{cond}}=1.D-4$. The accuracy is seen to be the best of all the results shown so far. If however, only an approximate solution is desired, the parameters of Fig.

13 are sufficient. The results seem to suggest that the accuracy depends primarily on the distance between the object boundary and the outer boundary provided that various quantities are calculated precisely. Twenty segments per wavelength, six layers, and an interlayer spacing of $\lambda/20$ seem to produce reasonable results for most cases. If G^* metrons are used, integration can be done using every other point.

Next, we consider an obstacle that has both concave and convex portions. A good candidate is the case of a gaussian hill for which results are available in the literature [18]. Such a hill has also been considered in [1]. The height of the hill, $h_g(x)$, over the $y = 0$ plane is given by

$$h_g(x) = Ae^{-[(x-B)/C]^2}.$$

We have chosen $A = C = 10\lambda/3$, $B = 0$. The obstacle is taken as the portion of the gaussian hill where the height exceeds $\lambda/100$. For the chosen parameters, this occurs for $|x| \lesssim 8\lambda$. The total arc length of the obstacle is about 18λ . The constitutive parameters of the earth are taken as $\epsilon_r = 10$, $\sigma = 10\text{mS/m}$ at a frequency of 1MHz. The latter corresponds to $\sigma_r = 180$. A vertically polarized source is located at $(-50\lambda/3, \lambda/100)$ to the left of the hill. Fig. 22 shows the incident magnetic field, H_{0z} , on the hill normalized to the free-space value. The dashed line corresponds to the field over a flat surface. The quantity $\delta\Pi$ in (42) has been calculated using (39) since $r_2 > 50$ on the obstacle. As expected, the field matches at the two ends of the obstacle with the field over a flat surface. In [18] the solution is obtained via Volterra type integral equation starting from parabolic approximation of the Helmholtz equation. By its very nature, the method of [18] considers one-way propagation and ignores backscattering. The present method, on the other hand, makes no such approximations. Fig. 23 compares the numerical solution of the present method with that of [18]. Both the G^* and the sinusoidal metron solutions have been obtained with 20 segments per wavelength node density, six layers, $h = 0.05\lambda$, and $R_{\text{cond}}=1.D-6$. For these values of parameters, the number of unknowns on the obstacle is 361. Full integration was employed in both cases. The solution obtained with G^* metrons agrees fairly well the results of [18], whereas the one with sinusoidal metrons is highly erroneous. The increased field strength on the illuminated side is due to focussing by

the concave portion of the hill. The G^* metron solution correctly predicts it. No such focussing is present in the incident field as can be observed from Fig. 22. Thus, physical optics cannot be expected to predict the correct field on the surface. It is to be noted that the erroneous result with sinusoidal metrons is not due to round off errors, for the G^* solution has a higher condition number and still produces a good result. This was also checked by repeating the numerical solution with various values of Rcond. The sinusoidal metron solution remained erroneous irrespective of the value of Rcond. In an attempt to improve the solution, a higher node density of 30 segments per wavelength was also tried. However, the solution only worsened. It is concluded that the sinusoidal metrons are not satisfactory for arbitrary shapes and that they do not lead to the correct values of the MEI coefficients. Choice of metrons is not arbitrary as the originators of the MEI method claim. The G^* metrons have a physical significance in that they represent the fields generated by line sources in an environment compatible with the original problem. No such statement can be made concerning the sinusoidal metrons.

It is interesting to compare the merits of the present method with G^* metrons *vis-à-vis* the method of [1] which solves the problem using a magnetic field integral equation and boundary element method. It took 5 minutes and 20 seconds on a 80486-50 PC to produce the results for the ground wave data shown in Fig. 5 as well as to generate sky wave data at 181 angles. Identical results were obtained with half integration which took only 3 minutes. This is in contrast to the method of [1] which took 75 minutes for the same problem. Of course [1] uses the free-space Green's function in contrast to the half-space Green's function employed here. The number of unknowns in [1] was 725 (obtained with 12 nodes per wavelength). For the same number of unknowns, the present method, being of order $O(N^2)$, would take about 21 minutes, which is still faster by a factor of about four. If half integration is used the method is faster by a factor of eight. The savings in memory in the present method are tremendous. For the problem at hand, the method of [1] with 725 unknowns requires a storage space of at least 8.4 MB compared to only 254 kB needed with the present method. To speed up the calculation of the Green's function we have assumed $\Delta_o = 0$ in (43). This amounts to assuming that the terrain outside the obstacle is made up of a perfect conductor. This results in substantial savings in time.

For example, it took 3 hours and 10 minutes on a 80486-50 PC to solve the problem of gaussian hill using the exact Green's function and half integration, compared to only 3 minutes with the approximate Green's function! The results were identical except near the right end of the hill where the two differed slightly. The value at $x - x_o = 160$ was 1.2 with the exact Green's function compared to about 0.9 with the approximate Green's function. One would expect the use of approximate Green's function to be the worst when Δ_o is significantly different from zero. We considered the case of highly lossy earth with $\epsilon_r = 5$ and $\sigma = 0.056\text{mS/m}$ at 1 MHz ($\sigma_r = 1$). A gaussian hill with $A = \lambda$, $B = 0$, and $C = 0.76\lambda$ was considered. A vertically polarized source is placed at $(-3\lambda, \lambda/10)$. Six layers were chosen with $h = 0.05\lambda$ and integration was performed utilizing all the nodes. Fig. 24 shows the calculations with the exact and the approximate Green's functions. The field that would exist on flat earth is also shown. Calculations with the exact Green's function took 30 seconds while those with the approximate Green's function took 45 minutes. However, it is seen that the results do not differ much from each other, justifying the use of the approximate Green's function.

It is possible to increase the accuracy of the numerical results shown in Fig. 23 by increasing the separation between the obstacle and the outer boundary. Fig. 25 shows calculations with 6, 8, and 10 layers all with $h = 0.05\lambda$. It is seen that the result with 10 layers is generally in best agreement with the results of [18]. The numbers indicated within the parenthesis in the caption are the values of Rcond assigned in each case to the first 15 wavelengths and the last 3 wavelengths respectively on the boundary. As discussed previously, the condition number increases generally as the separation is increased. We selectively filter out the singular vectors which are highly corrupted by roundoff errors by choosing a higher value of Rcond. The far-zone fields are however insensitive to the slight variations of the surface fields. Fig. 26 shows the relative pattern of the source with 6 and 8 layers. It is seen that the two cases produce virtually the same results. The radiation pattern of the source in the direction of the hill is highly perturbed by the presence of the latter. Away from the hill the relative pattern in the presence of the hill is not very different from the pattern of a vertical source in free-space except near grazing angles where it has a deep minimum.

Finally, we present results on the effect of relative location of the source with respect to the obstacle on the fields. A vertically polarized source was placed near a gaussian hill having $A = 1.2\lambda$, $B = 0$, and $C = \lambda$. The total arc length of the obstacle is 5.1λ . The ground constants were $\epsilon_r = 14.9$, $\sigma_r = 14.58$. Six layers with 20 segments per wavelength, and $h = 0.05\lambda$ were chosen in the numerical model. In one case the source was placed at the bottom of the hill at a horizontal distance of 4.53λ from the peak. In the second case the source was placed at the top of the hill ($x_0 = 0$). Fig. 27 shows the normalized ground wave on the hill. Once again there is focussing on the illuminated side of the hill when the source is at the bottom. The field for the source at the top of the hill is symmetric as expected. Note that the field in the shadow region of the hill for $x_0 = -4.53\lambda$ is as strong as the corresponding field for $x_0 = 0$. There is no apparent advantage of siting the antenna at the top of the hill to receive the ground wave. However, the radiation pattern of the source from $\phi = 0$ to 90° is significantly affected by the presence of the hill. This can be seen from Fig. 28 which shows the relative pattern for the two source locations. Irrespective of the source location, the radiation pattern has a deep minimum near grazing angles as is characteristic of vertical antennas over lossy earth.

IV. SUMMARY

A fast, finite difference method that includes all aspects of wave phenomenon such as reflection, refraction, diffraction, and backscattering is presented for predicting two dimensional propagation over inhomogeneous, irregular terrain. The terrain is characterized by its elevation and impedance, which, in turn depends on the ground constants of the earth. Both of these may vary with distance. The terrain topology data is specified at discrete points. Interpolation using quadratic elements is done to define a continuous geometry. The computational domain for the problem consists of the area bounded by the terrain at the bottom and a truncating boundary at the top. To simulate free-space on the truncating boundary, discrete, near-field radiation condition of Mei type, derivable from an integral representation of the fields, is imposed. Green's function for half-space is used to reduce the number of unknowns. Unknowns are distributed on the terrain only where its elevation is non-zero and/or where its impedance differs from a reference value. The computational domain is discretized using interior layers between the truncating and the object boundaries. Finite difference coefficients valid for an irregular, non-orthogonal mesh are presented. Accurate expressions are provided for the Green's function and incident fields over a constant-impedance, flat plane. The expressions permit rapid computation as they do not involve the troublesome Sommerfeld integrals. Results are presented for the ground wave as well as the sky wave.

The truncating boundary can be in the near-field of the obstacle; as near as a $\lambda/4$ away from it, and the method works both for concave and convex geometries. Good results have been obtained with a node density of about 20 per wavelength and an interlayer spacing of about $\lambda/20$. The metrons used for the determination of the Mei coefficients are proportional to the complex conjugate of the Green's function and fully accommodate the environment of the problem. Singular value decomposition which permits filtering of the space spanned by the corrupted singular vectors is used to solve for the coefficients.

The method is attractive for large terrain obstacles where other methods tend to be slow. The overall computational time of the method is of order $O(N^2)$. Storage requirements are of order $O(N)$, where N is the total number of unknowns (nodes). As an example, for a terrain obstacle extending over 18 wavelengths, the number of nodes on the

boundary is 361. To compute ground wave data at all of these nodes as well as to compute the far-fields at 181 angles, the method takes around 3 minutes on a 80486-50 PC. The total storage required for the problem is around 254 kB. It would take around 300 minutes with a storage space of around 2.5 MB to solve the problem of a terrain where the obstacle extends over 180 wavelengths. At a frequency of 1 MHz the terrain obstacle corresponds to one whose arc length is 54 km. At a frequency of 1 GHz it corresponds to an arc length of 54 m.

Certain spurious oscillations and over estimation of the field have been observed in some regions of the shadow region. This is attributed to the fact that it is difficult to calculate near-fields precisely over an electrically small, discrete domain. These extraneous effects can be somewhat reduced by increasing the separation between the obstacle and the truncating boundary. It is speculated that they can be further reduced by choosing a computational molecule that accommodates higher order derivatives. More efficient schemes of evaluating the Green's function and the near-fields will have to be made to further reduce the computational time.

Extension to the three dimensional case is trivial in principle, although not so computationally. Savings over integral equation methods will be even more dramatic in the case of three dimensional obstacles. Although the Green's function using complex images will be little more involved than for the two-dimensional case, it will have the computational advantage of being expressible in terms of an exponential functions instead of Hankel functions with complex arguments. The fields decay more rapidly with distance in three dimensions than in two dimensions. As a result integration could be done little more efficiently in the former case. The corresponding computational molecule will now consist of seven nodes instead of five in two dimensions. Finite difference and terminating boundary conditions will have to be developed for vector fields instead of scalar fields. These task are presently being pursued.

REFERENCES

- [1] R. Janaswamy, "A Fredholm integral equation method for propagation predictions over small terrain irregularities," *IEEE Trans. Antennas Propagat.*, vol. 40, no. 11, pp. 1416-1422, November 1992.
- [2] C. A. Balanis, *Advanced Engineering Electromagnetics*. New York: John Wiley & Sons, 1989.
- [3] S. Marcus, "A finite difference method for propagation predictions over irregular terrain," Joint IEEE AP-S International Symposium and URSI Meeting, London, Ontario, Canada, July 1991.
- [4] K. K. Mei, R. Pous, Z. Chen, and Y. W. Liu, "The measured equation of invariance: A new concept in field computation," Joint IEEE AP-S International Symposium and URSI Radio Science Meeting, Chicago, IL, July 1992.
- [5] A. Bayliss, M. Gunzburger, and E. Turkel, "Boundary conditions for the numerical solution of elliptic equations in exterior regions," *SIAM Journal of Applied Math.*, vol. 42, no. 2, pp. 430-451, April 1982.
- [6] R. Janaswamy, "2-D radiation boundary conditions for an arbitrary outer boundary," *Microwave and Optical Technology Letters*, vol. 5, no. 8, pp. 393-395, July 1992.
- [7] L. W. Pearson, R. A. Whitaker, and J. Bahrmassel, "An exact boundary condition for the finite element solution of electromagnetic scattering," *IEEE Trans. Magnetics*, vol. 25, no. 4, pp. 3046-3048, July 1989.
- [8] R. E. Stovall and K. K. Mei, "Application of a unimoment technique to a biconical antenna with inhomogeneous dielectric loading," *IEEE Trans. Antennas Propagat.*, vol. AP-23, no. 3, pp. 335-342, May 1975.
- [9] T. B. A. Senior, "Impedance boundary conditions for imperfectly conducting surfaces," *Appl. Sci. Res.*, sec B, vol. 8, pp. 418-436, 1960.
- [10] R. Pous, *The Measured Equation of Invariance: A New Concept in Field Computation*, Ph.D. Dissertation, University of California, Berkeley, 1992.
- [11] A. Sommerfeld, *Partial Differential Equations in Physics*. New York: Academic Press, 1949.
- [12] I. V. Lindell and E. Alanen, "Exact image theory for the Sommerfeld half-space problem, part I: vertical magnetic dipole," *IEEE Trans. Antennas Propagat.*, vol. AP-32, no. 2, pp. 126-133, February 1984.
- [13] Y. L. Chow, J. J. Yang, D. G. Fang, and G. E. Howard, "A closed form spatial Green's function for the thick microstrip substrate," *IEEE Trans. Microwave Theory Tech.*, vol. MTT-39, no. 3, pp. 588-592, March 1991.
- [14] F. B. Hildebrand, *Introduction to Numerical Analysis*. New York: Dover Publications, p. 457, 1987.
- [15] C. F. du Toit, "The numerical computation of Bessel functions of the first and second kind for integer orders and complex arguments," *IEEE Trans. Antennas Propagat.*, vol. 38, no. 9, pp. 1341-1349, September 1990.
- [16] J. Jetvic and R. Lee, "A theoretical and numerical analysis of the measured equation of invariance," submitted to *IEEE Trans. Antennas Propagat.*, June 1993.

- [17] E. Angels, "Invariant imbedding, difference equations, and elliptic boundary value problems," *J. Comp. Syst. Sci.*, vol. 4, pp. 473–491, 1970.
- [18] R. H. Ott, "An alternative integral equation for propagation over irregular terrain, 2" *Radio Science* , vol. 6, no. 4, pp. 429–435, April 1971.
- [19] G. H. Golub and C.F. Van Loan, *Matrix Computations*. Baltimore: John Hopkins University Press, 1983.
- [20] C. A. Brebbia and S. Walker, *Boundary Element Techniques in Engineering*. London: Newnes-Butterworths, 1980.
- [21] M. Abramowitz and I. A. Stegun, *Handbook of Mathematical Functions*. New York: Dover, 1965.

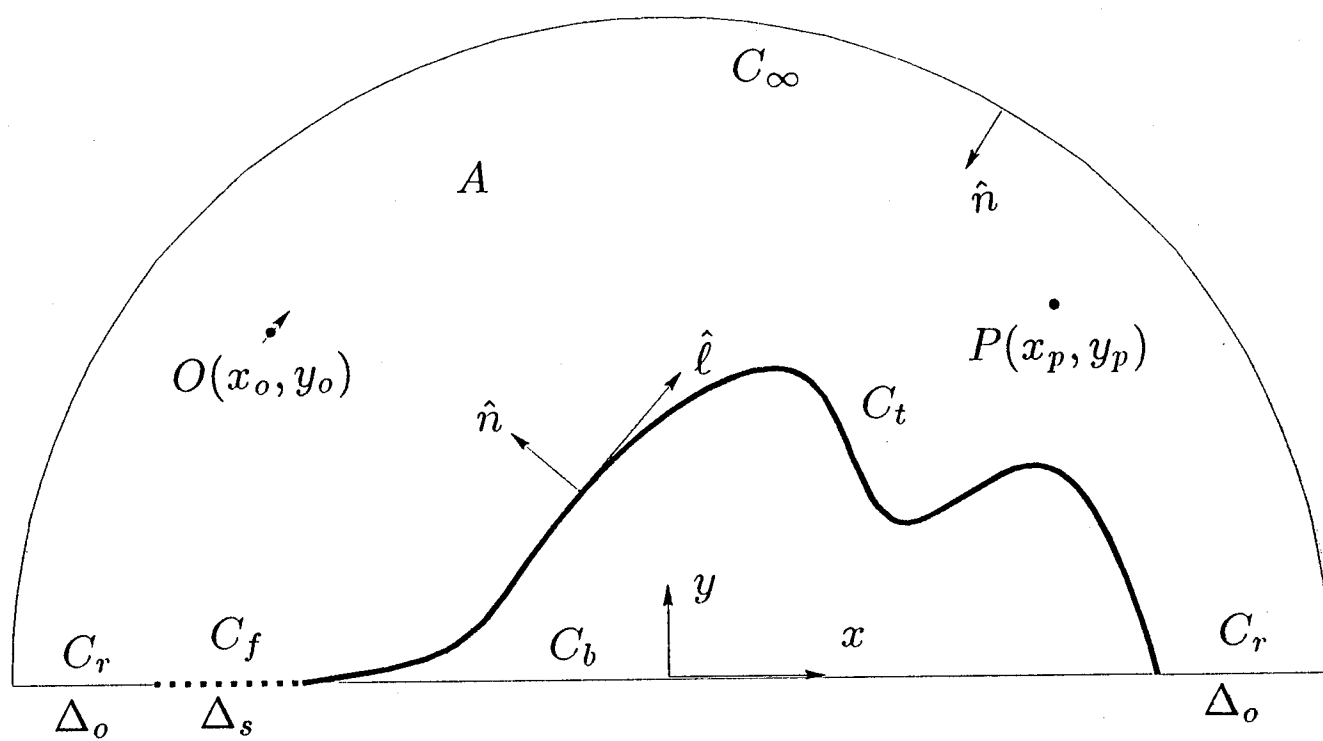


FIG. 1.

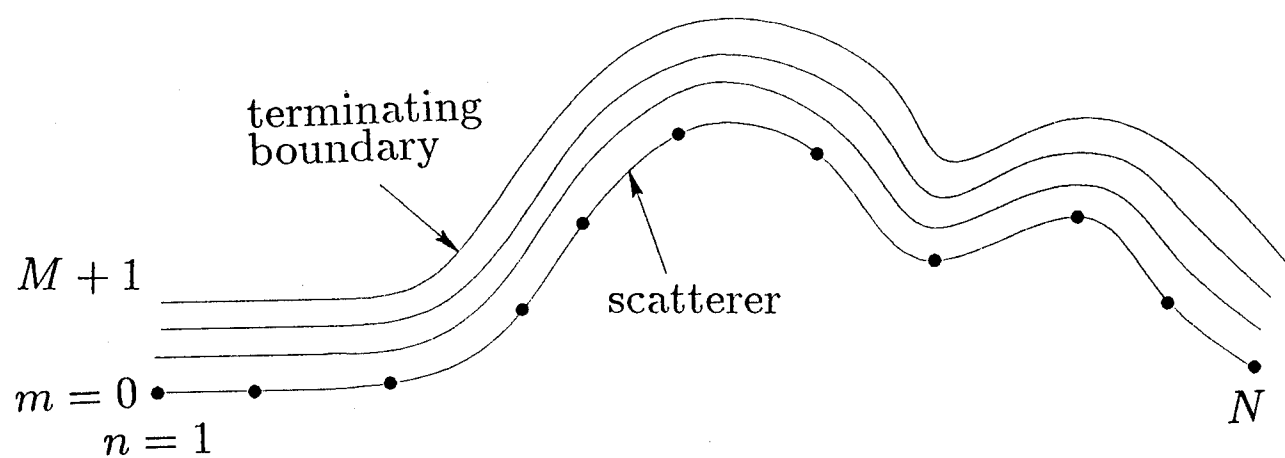


FIG. 2.

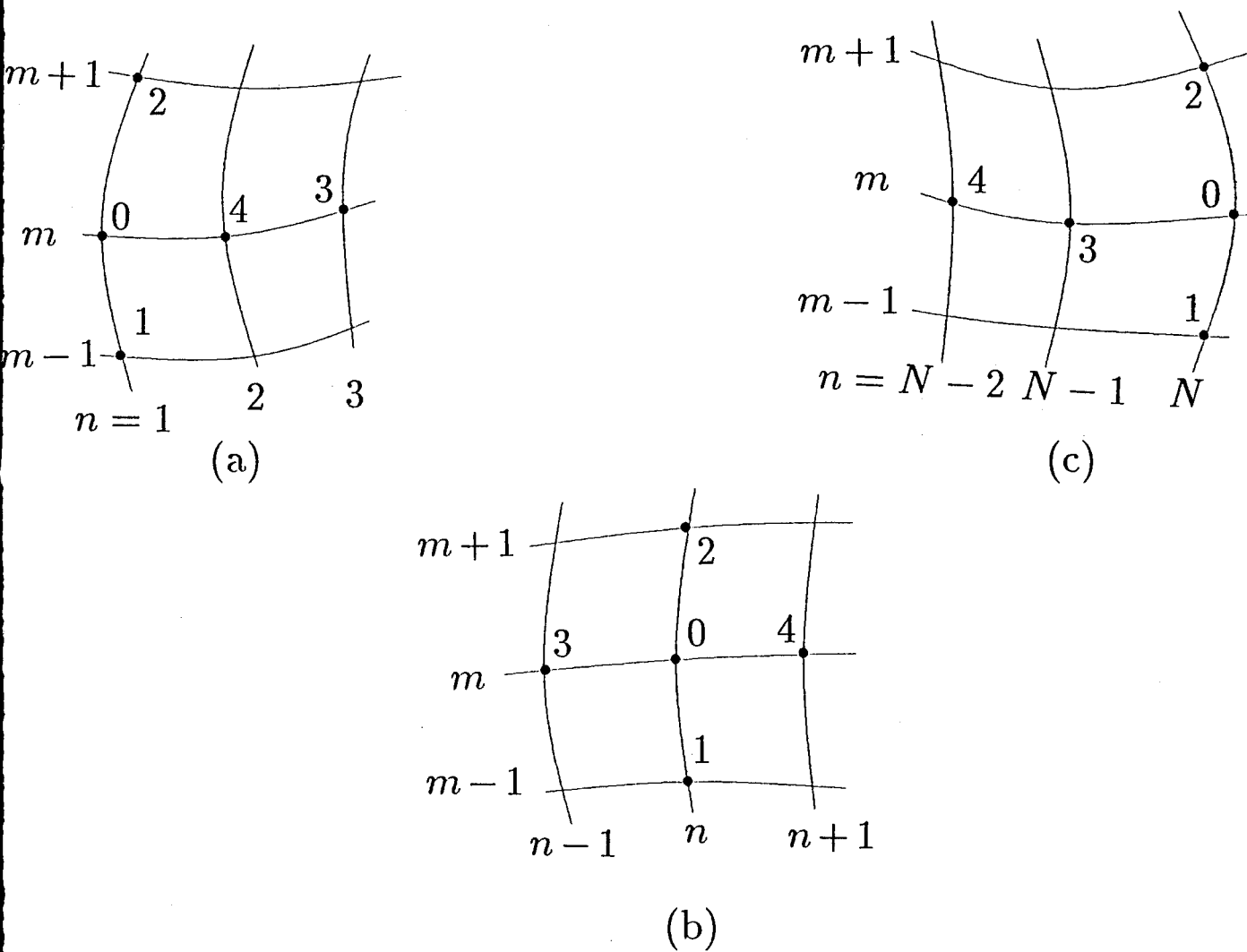


FIG. 3.

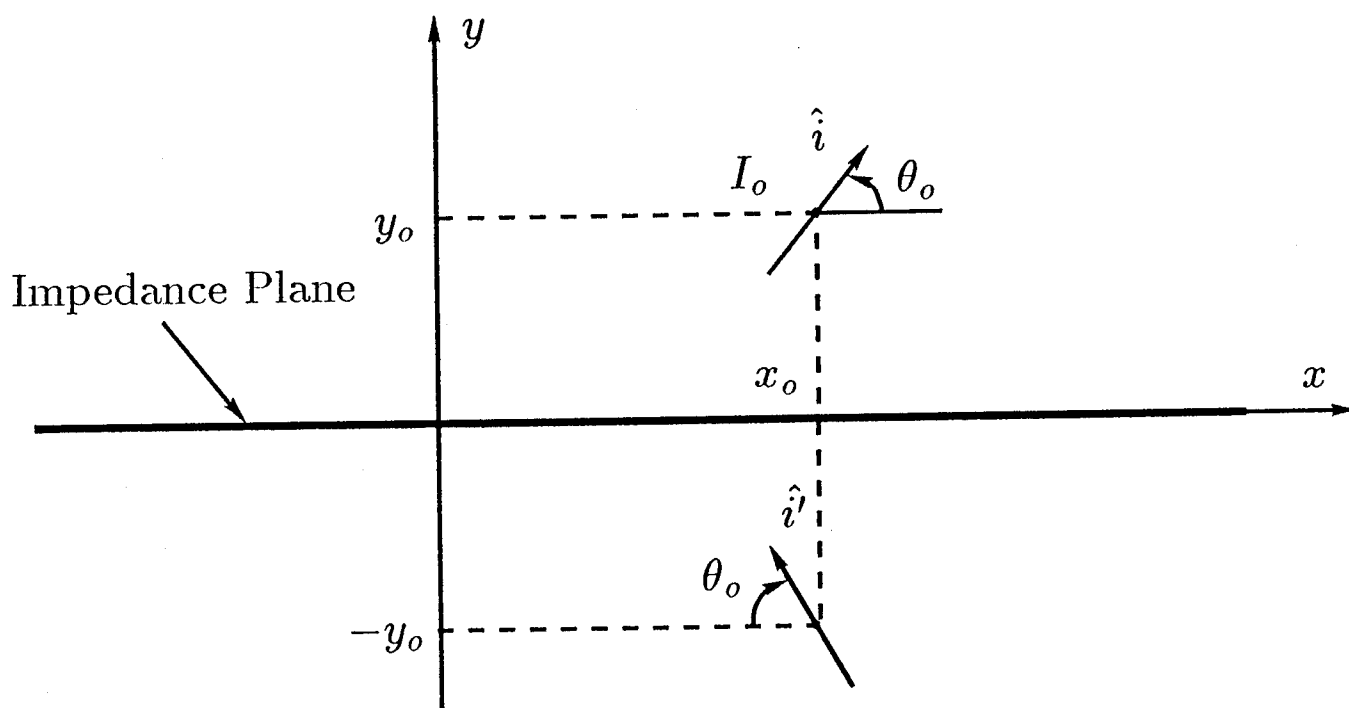


FIG. 4.

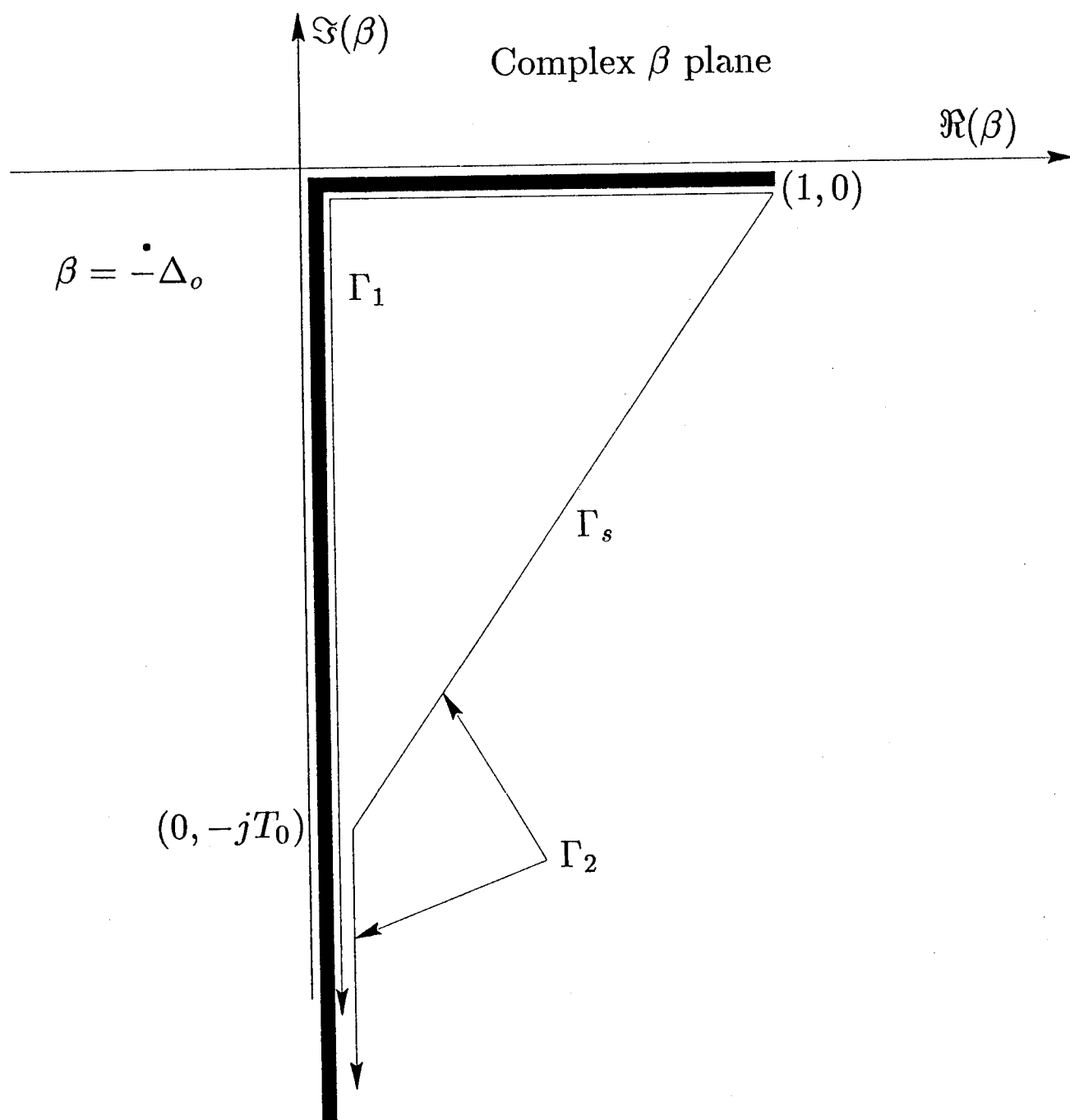


FIG. 5.

Surface Magnetic Field on Lossy Flat Earth

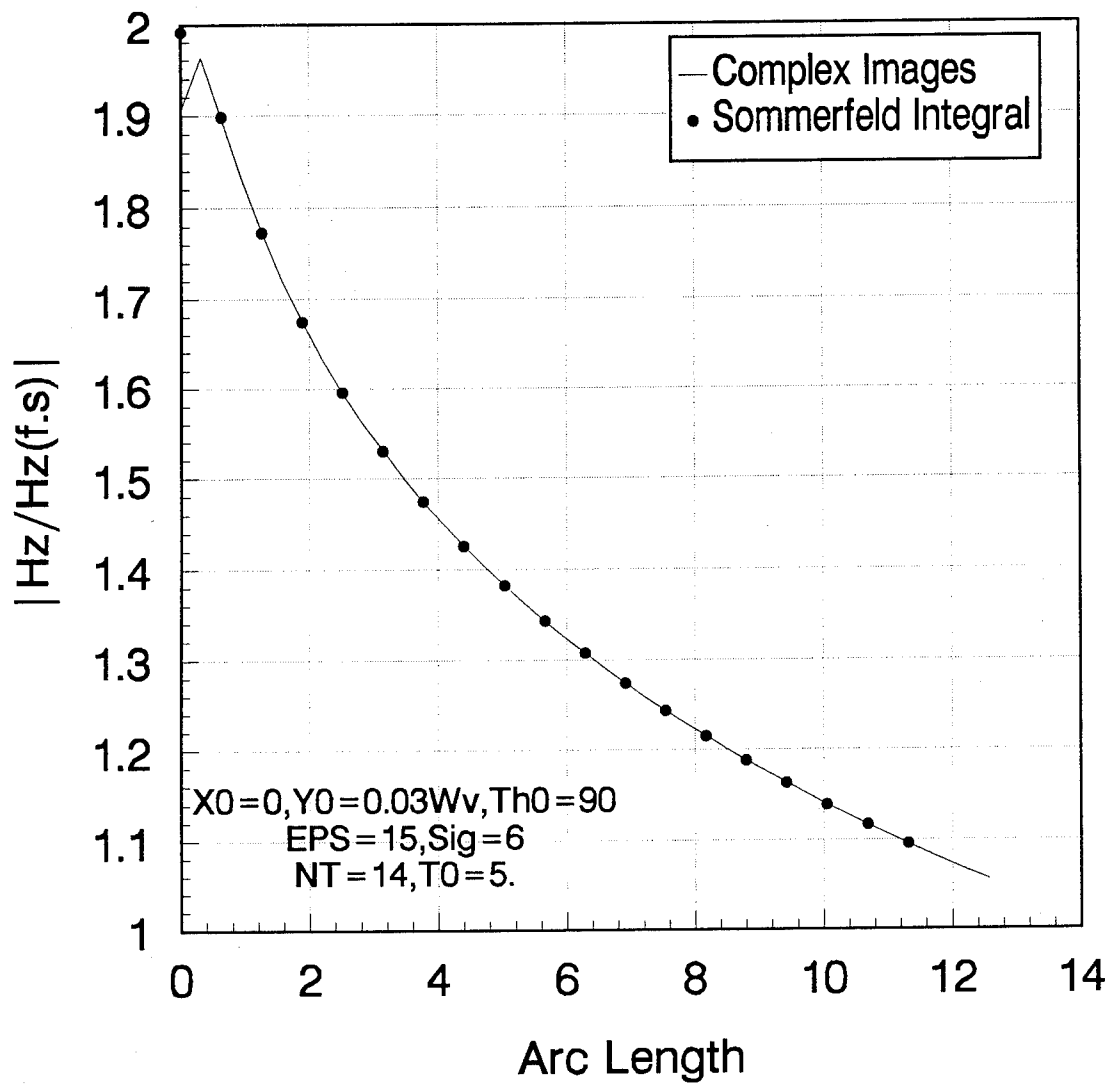


FIG. 6.

Surface Magnetic Field on Circular Boss

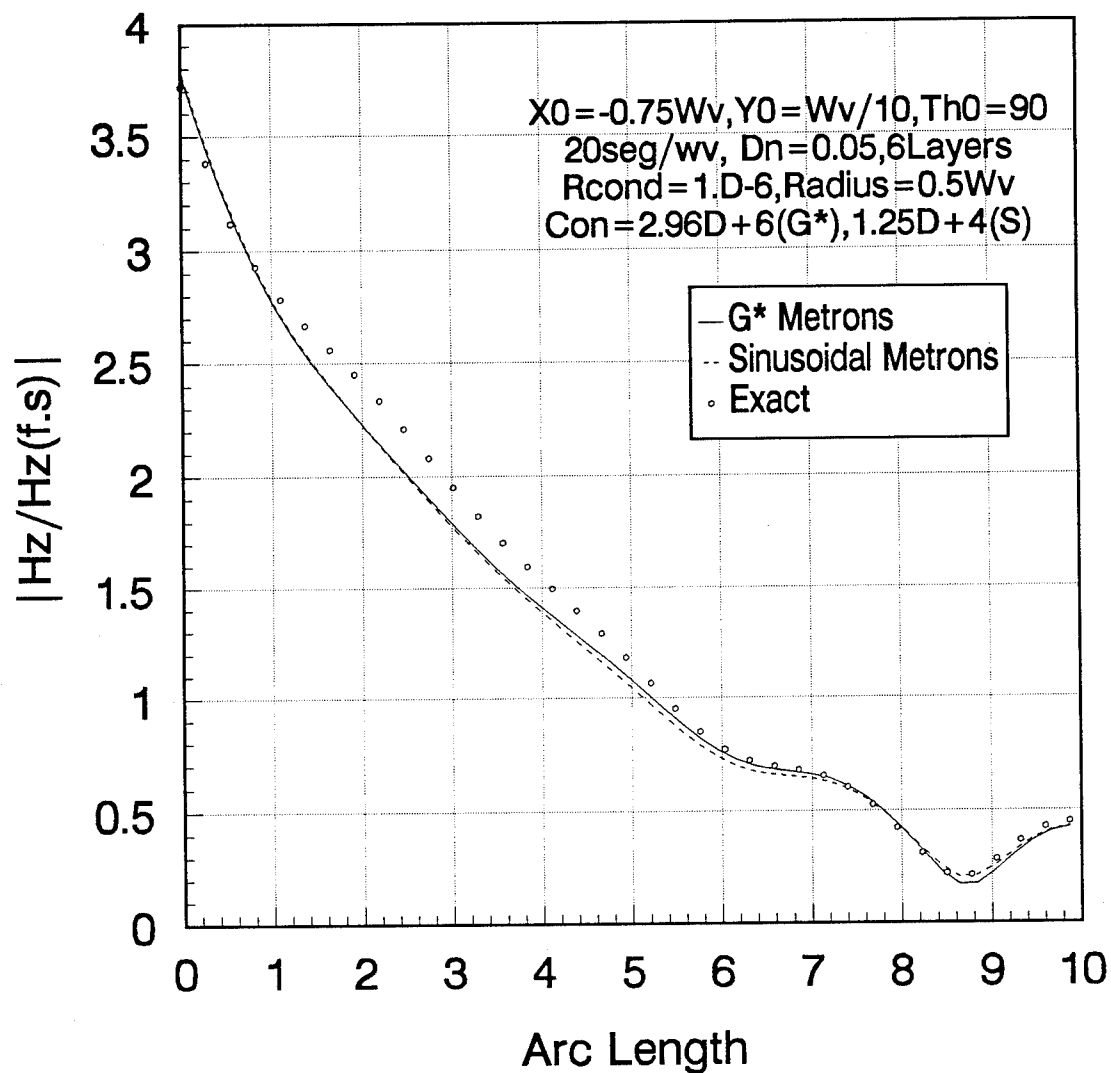


FIG. 7.

Source Pattern Near Circular Boss

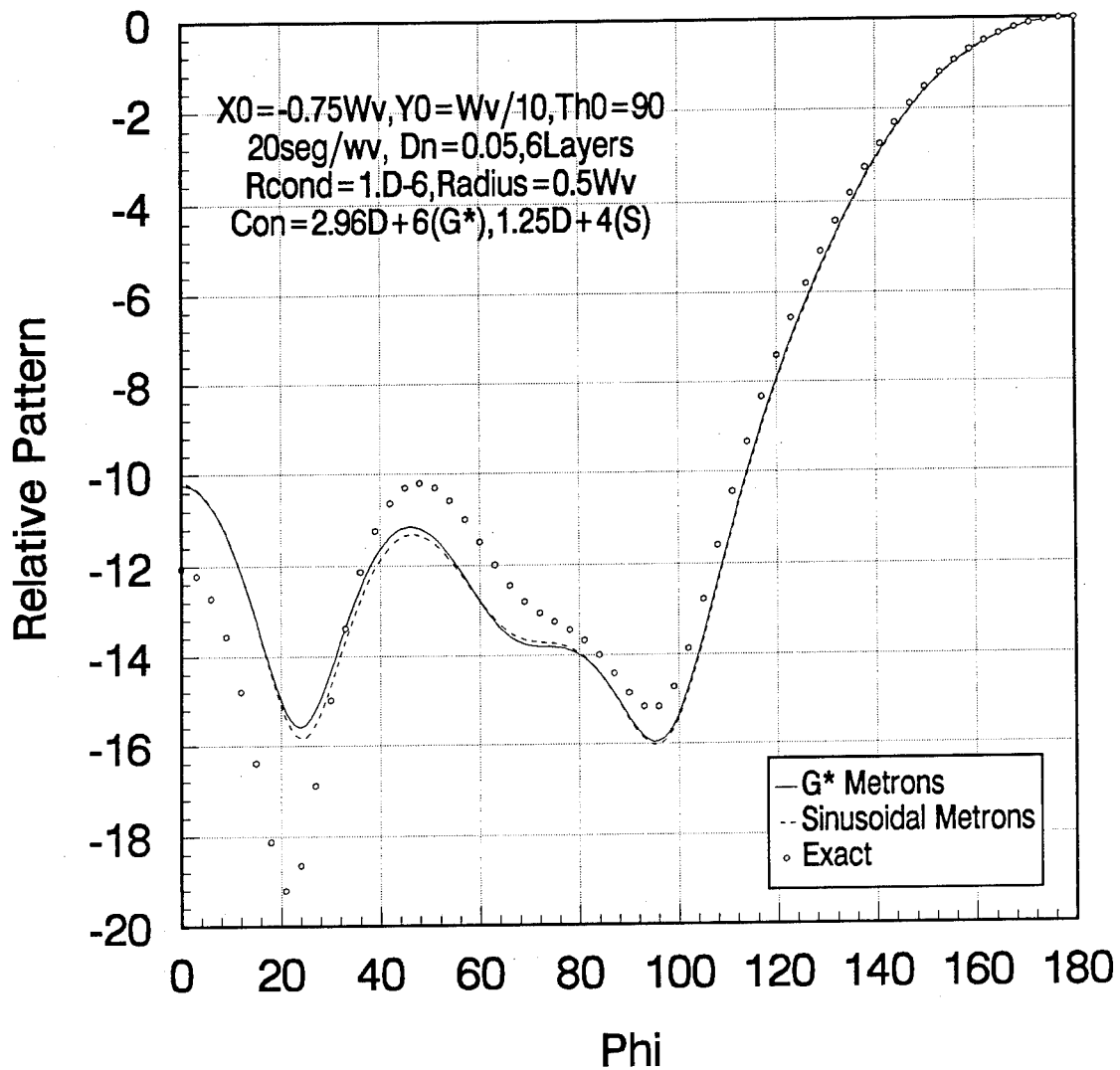


FIG. 8.

Surface Magnetic Field on Circular Boss

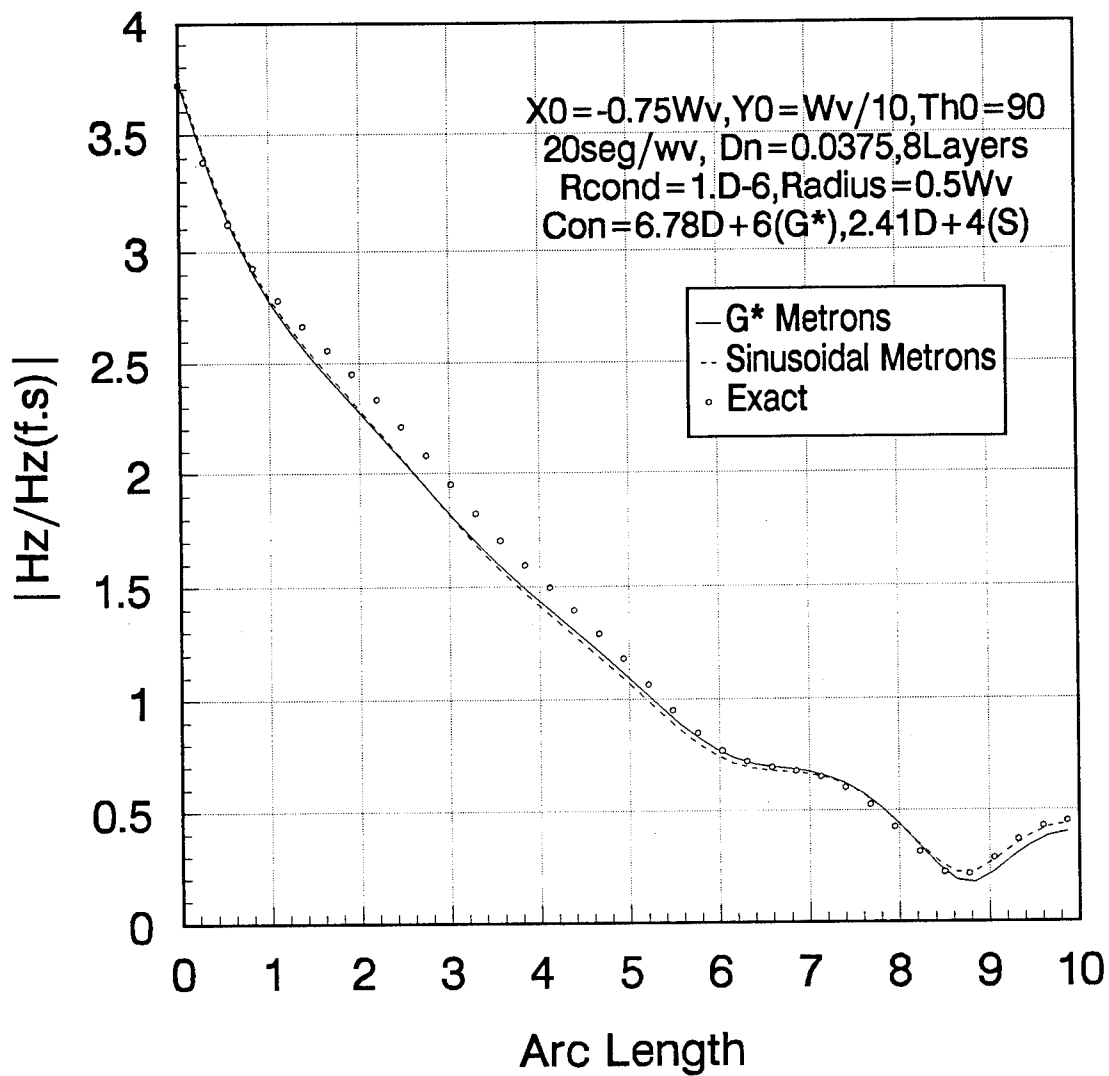


FIG. 9.

Surface Magnetic Field on Circular Boss

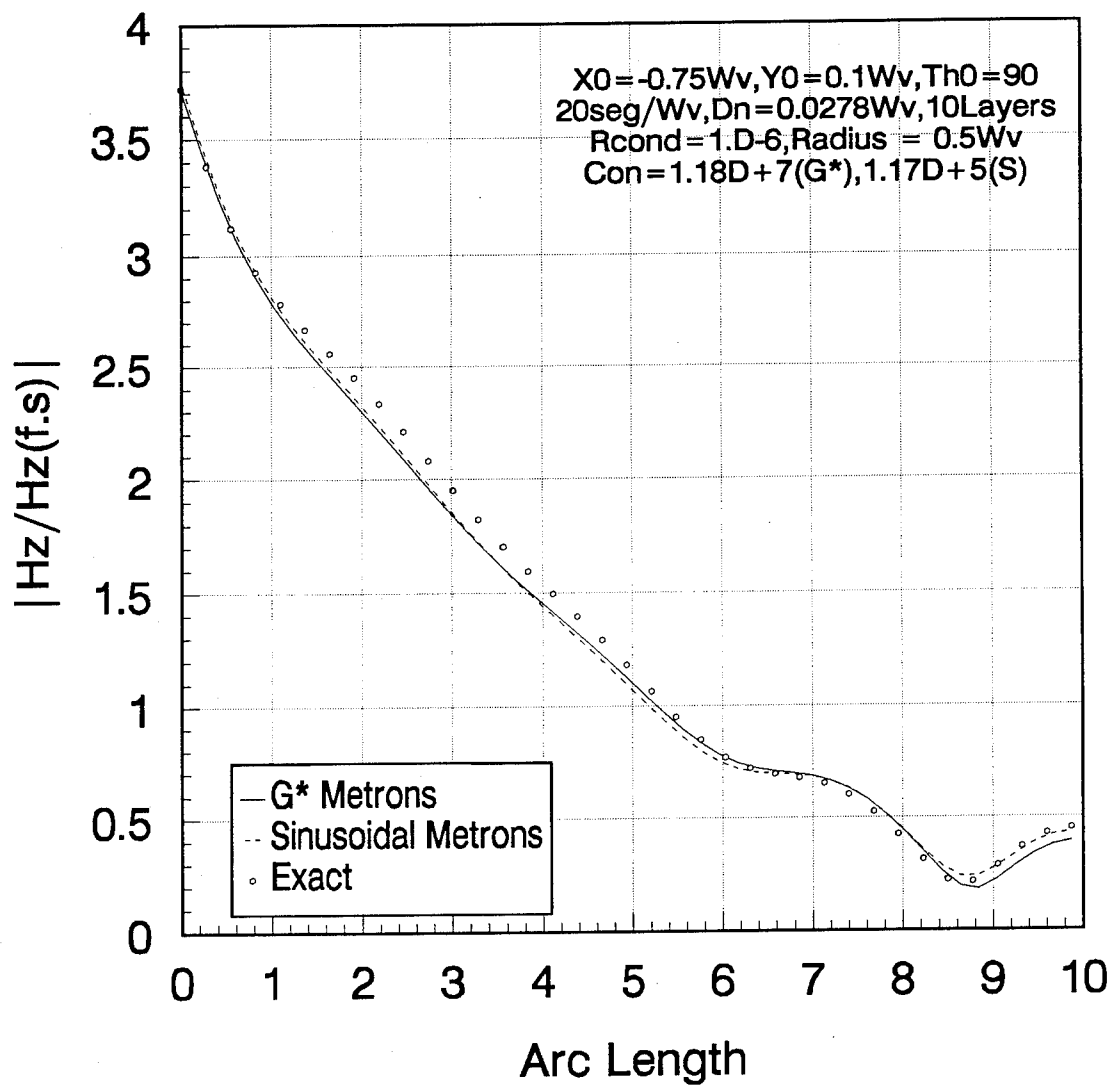


FIG. 10.

Surface Magnetic Field on Circular Boss

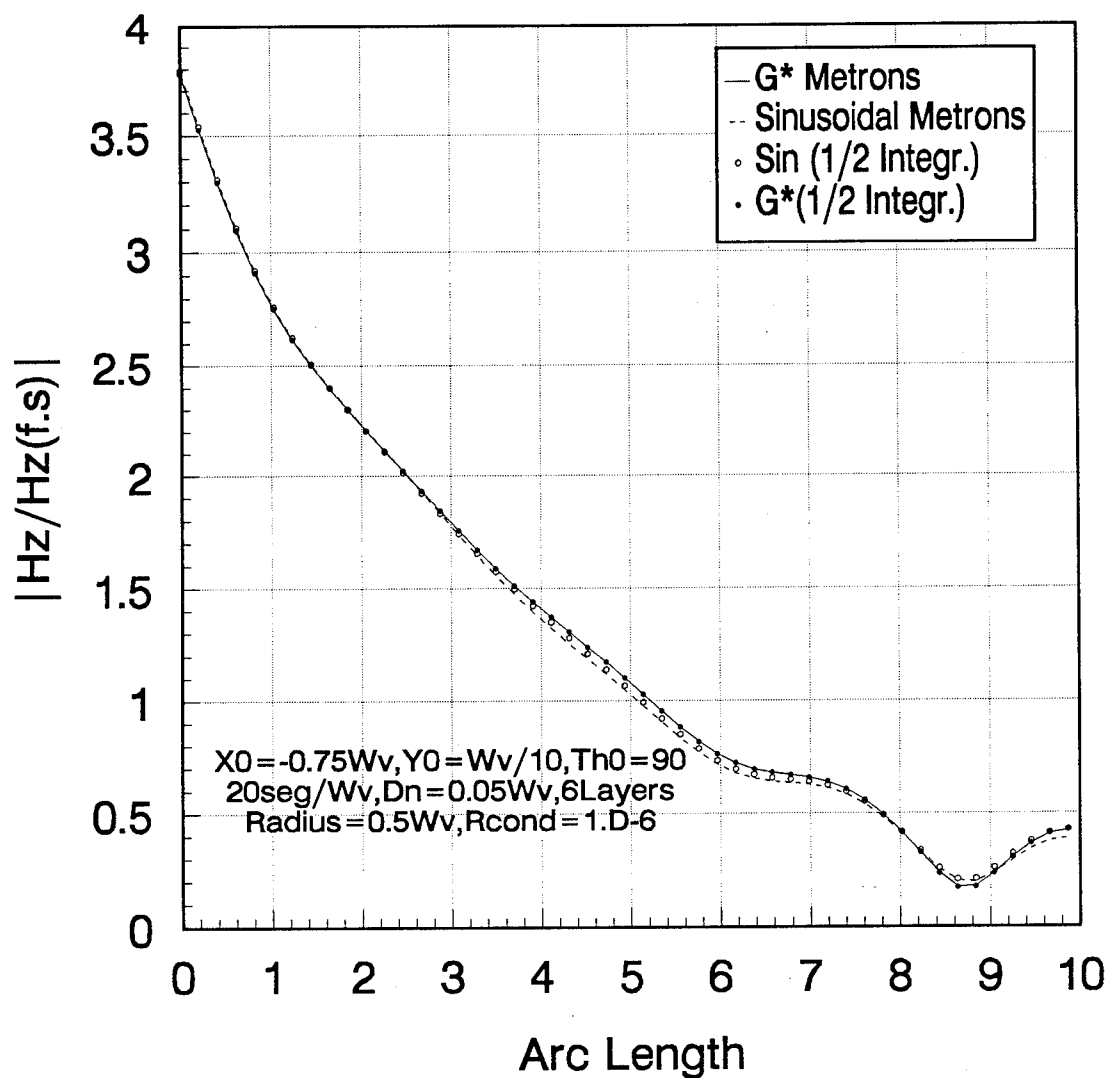


FIG. 11.

Surface Magnetic Field on Circular Boss

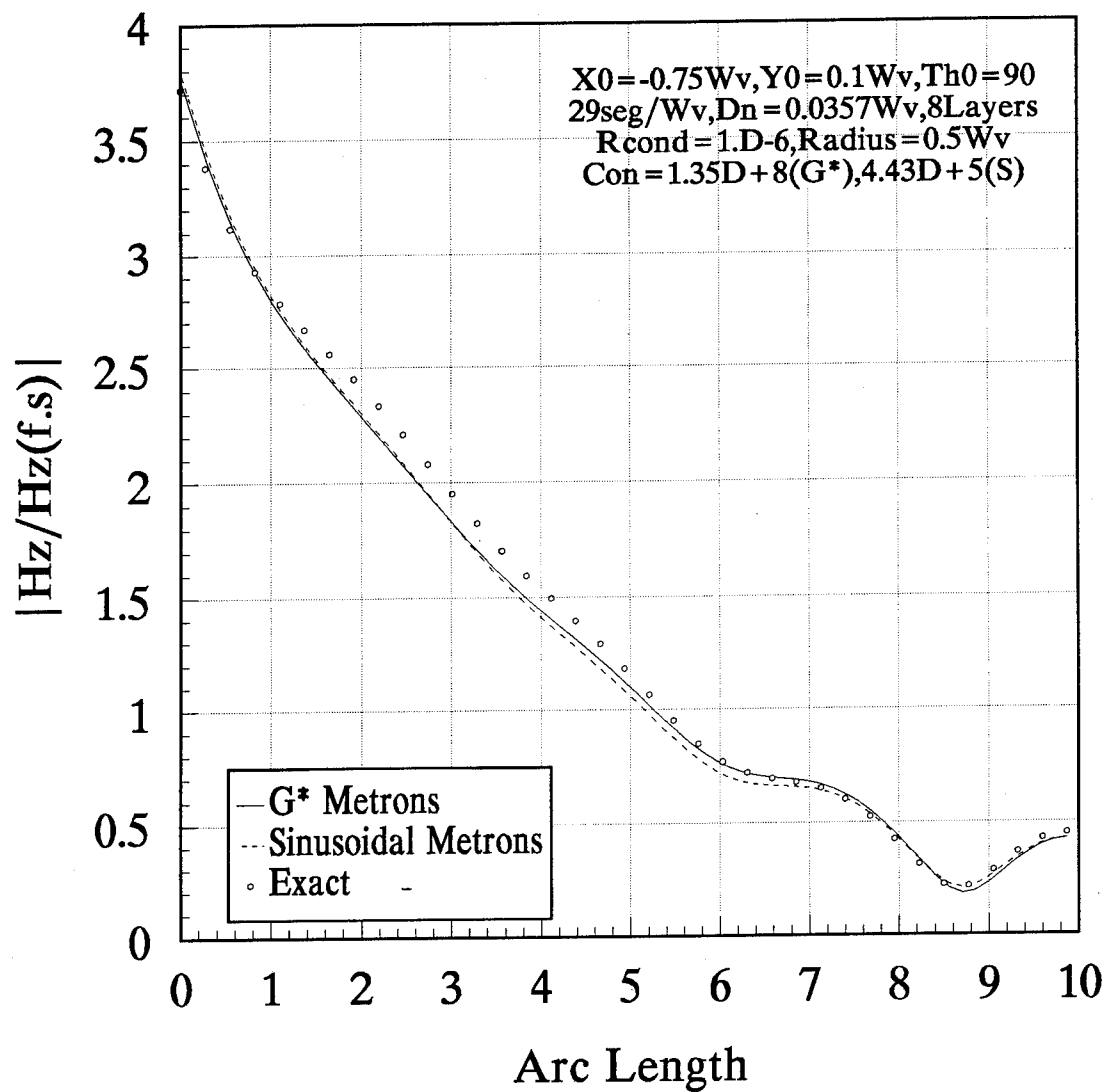


FIG. 12

Surface Magnetic Field on Circular Boss

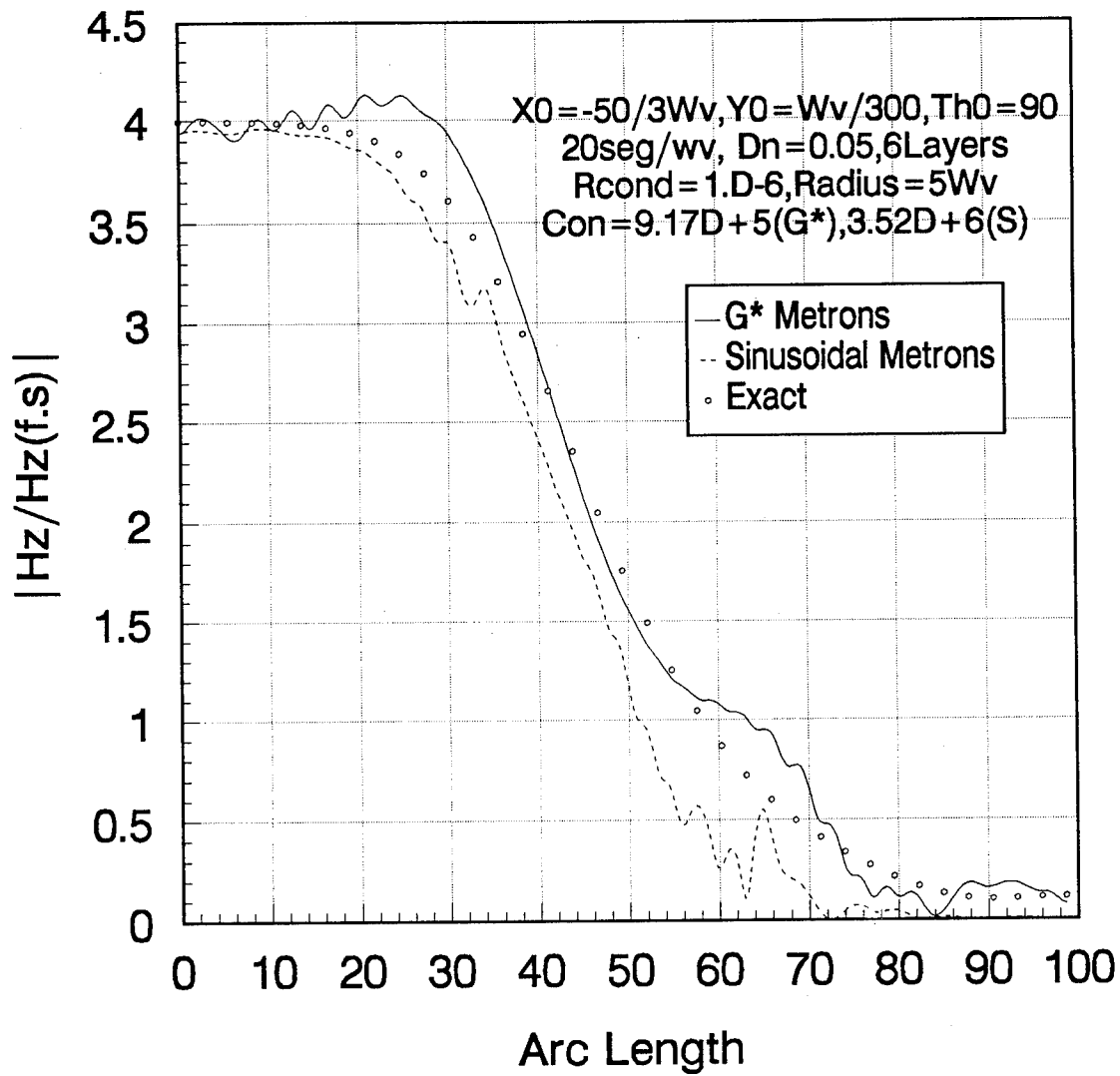


FIG. 13.

Source Pattern Near Circular Boss

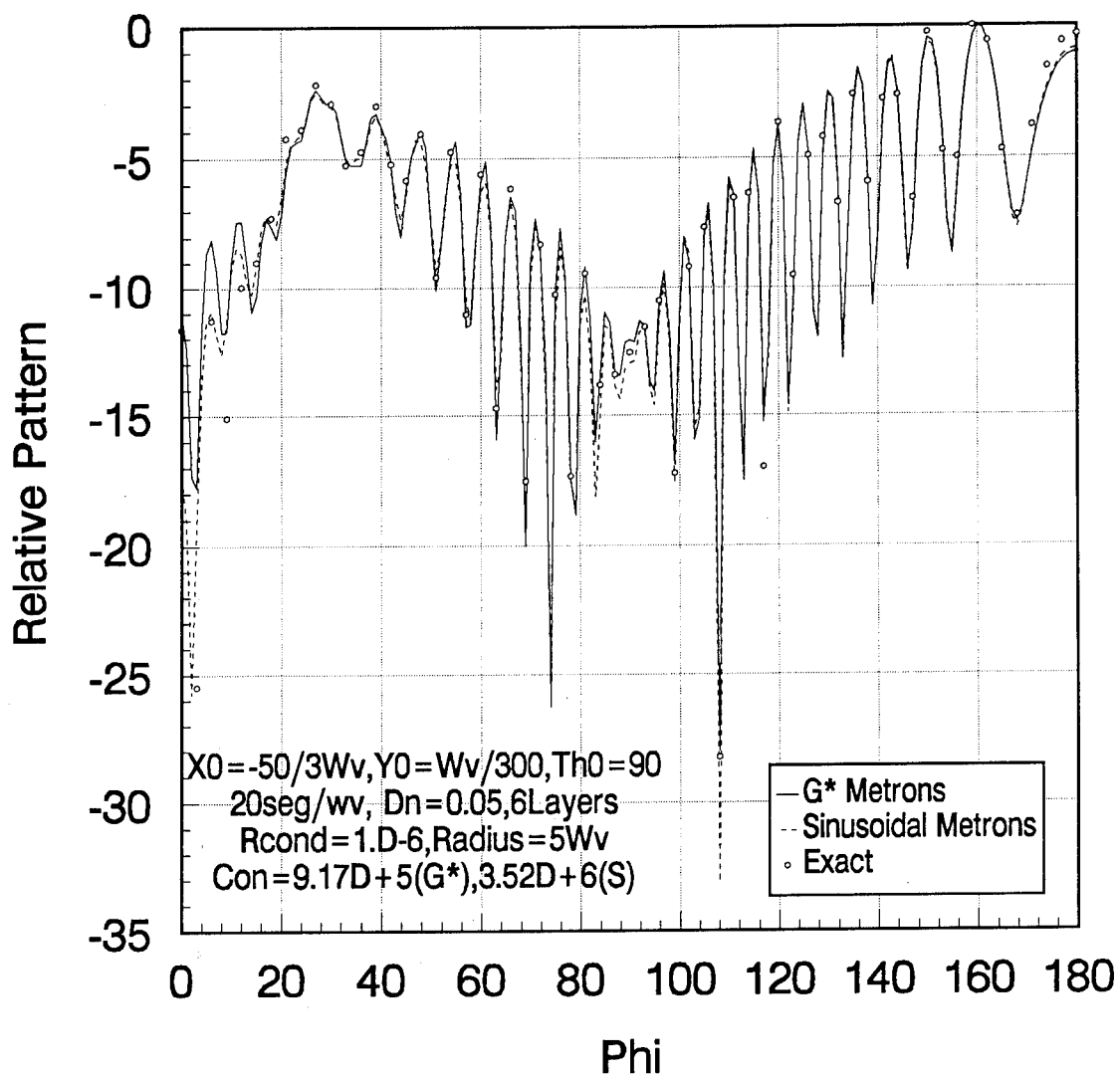


FIG. 14.

Surface Magnetic Field on Circular Boss

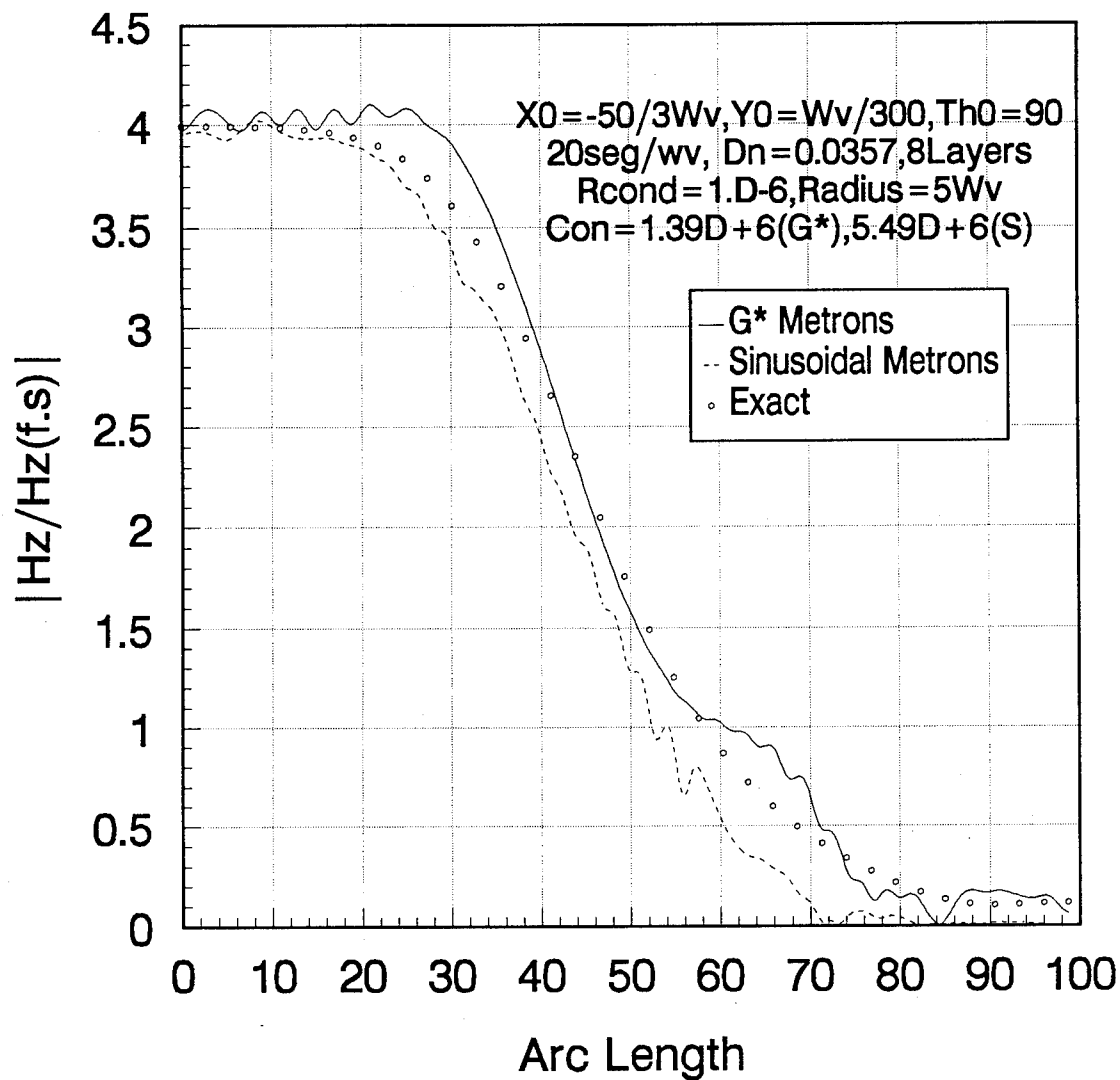


FIG. 15.

Surface Magnetic Field on Circular Boss

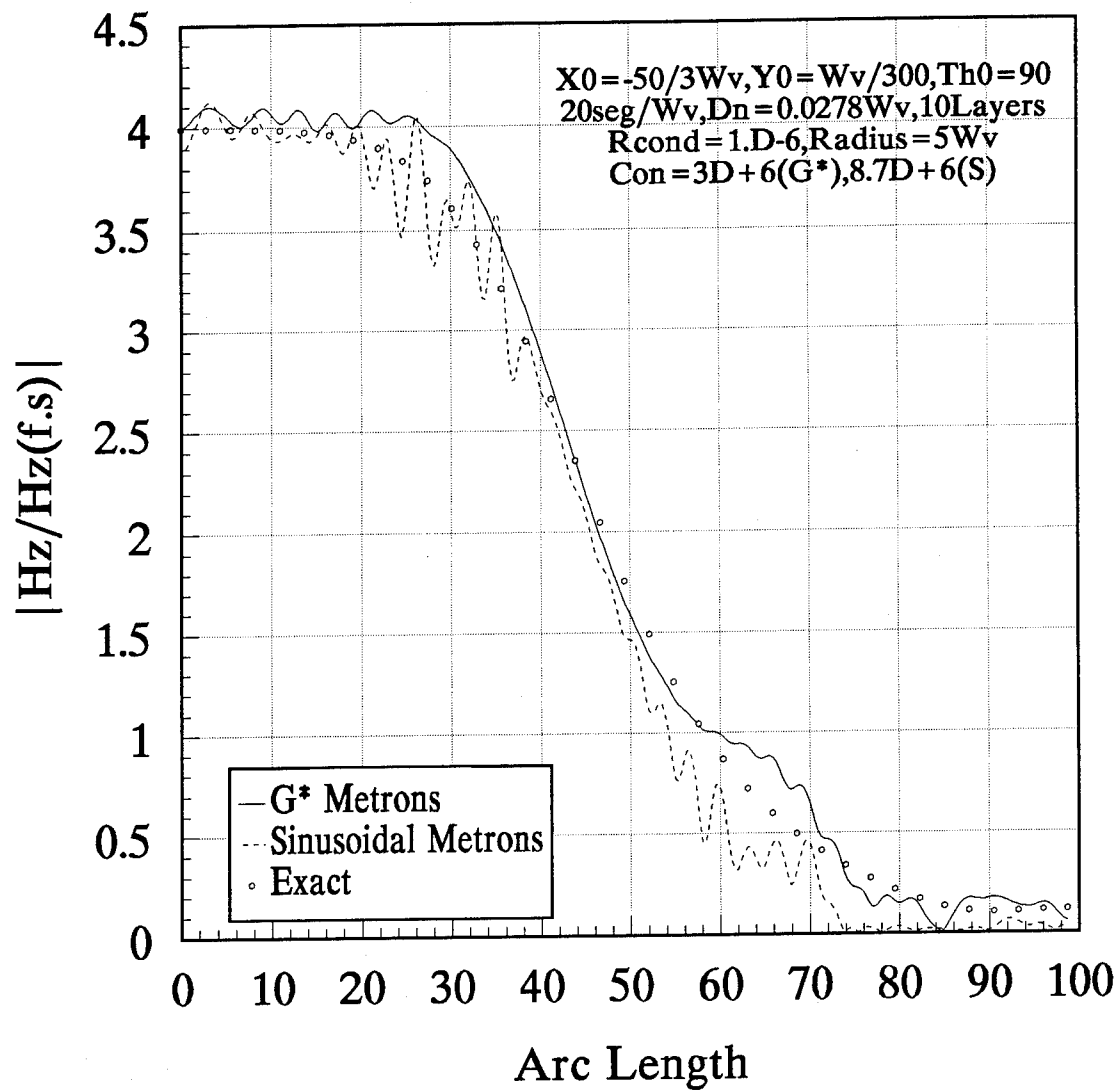


FIG. 16.

Surface Magnetic Field on Circular Boss

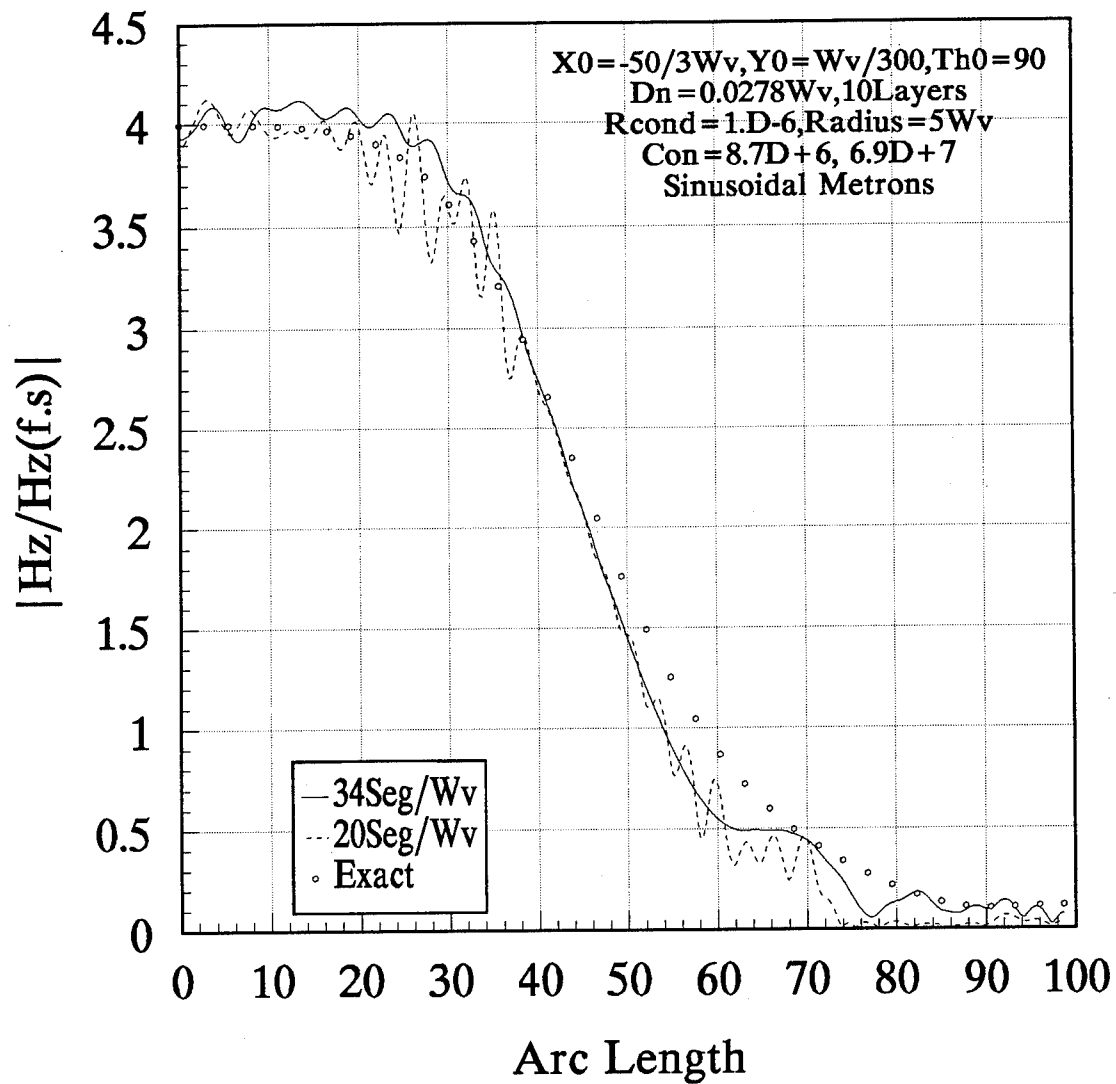


FIG. 17.

Surface Magnetic Field on Circular Boss

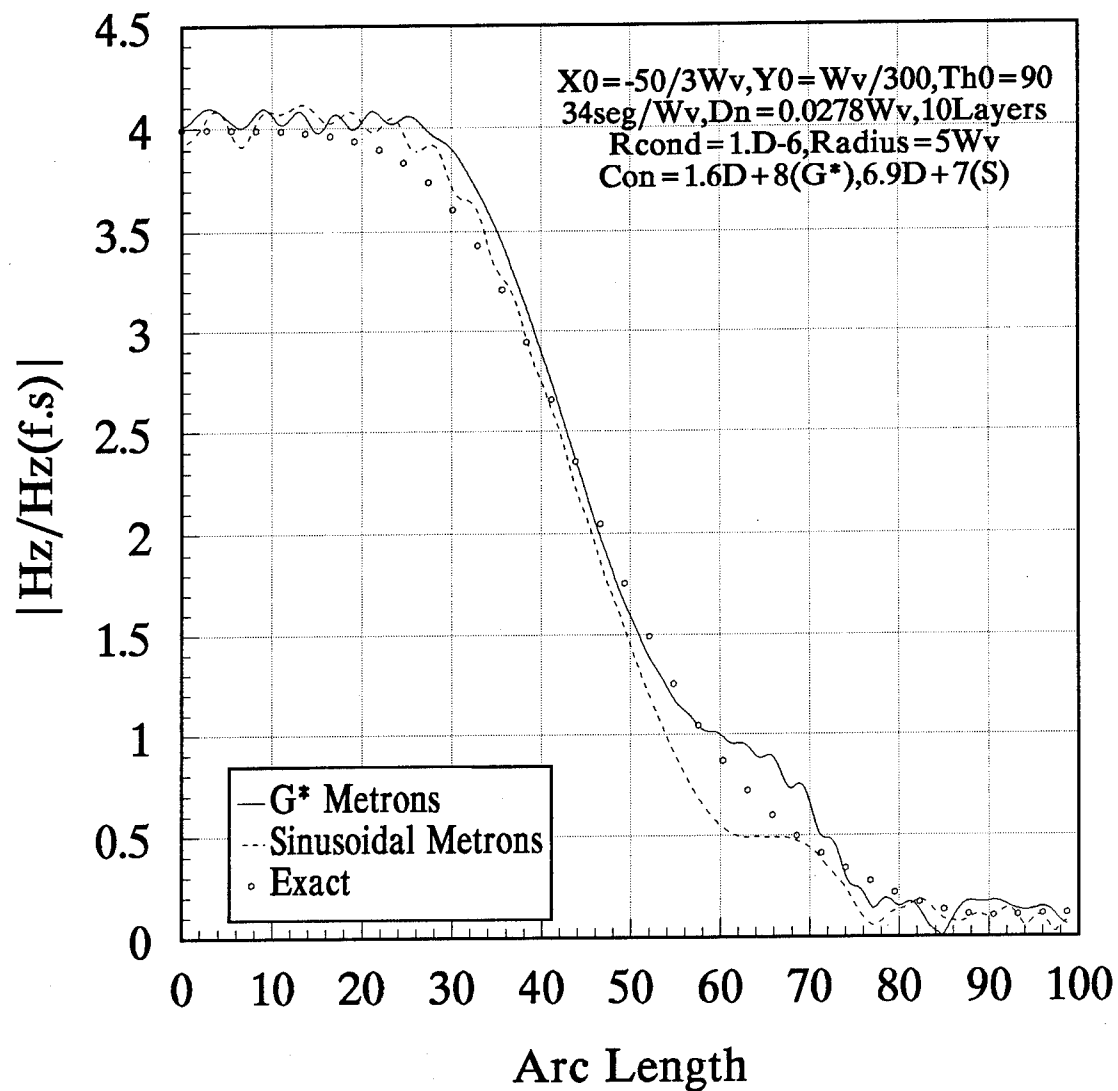


FIG. 18.

Surface Magnetic Field on Circular Boss

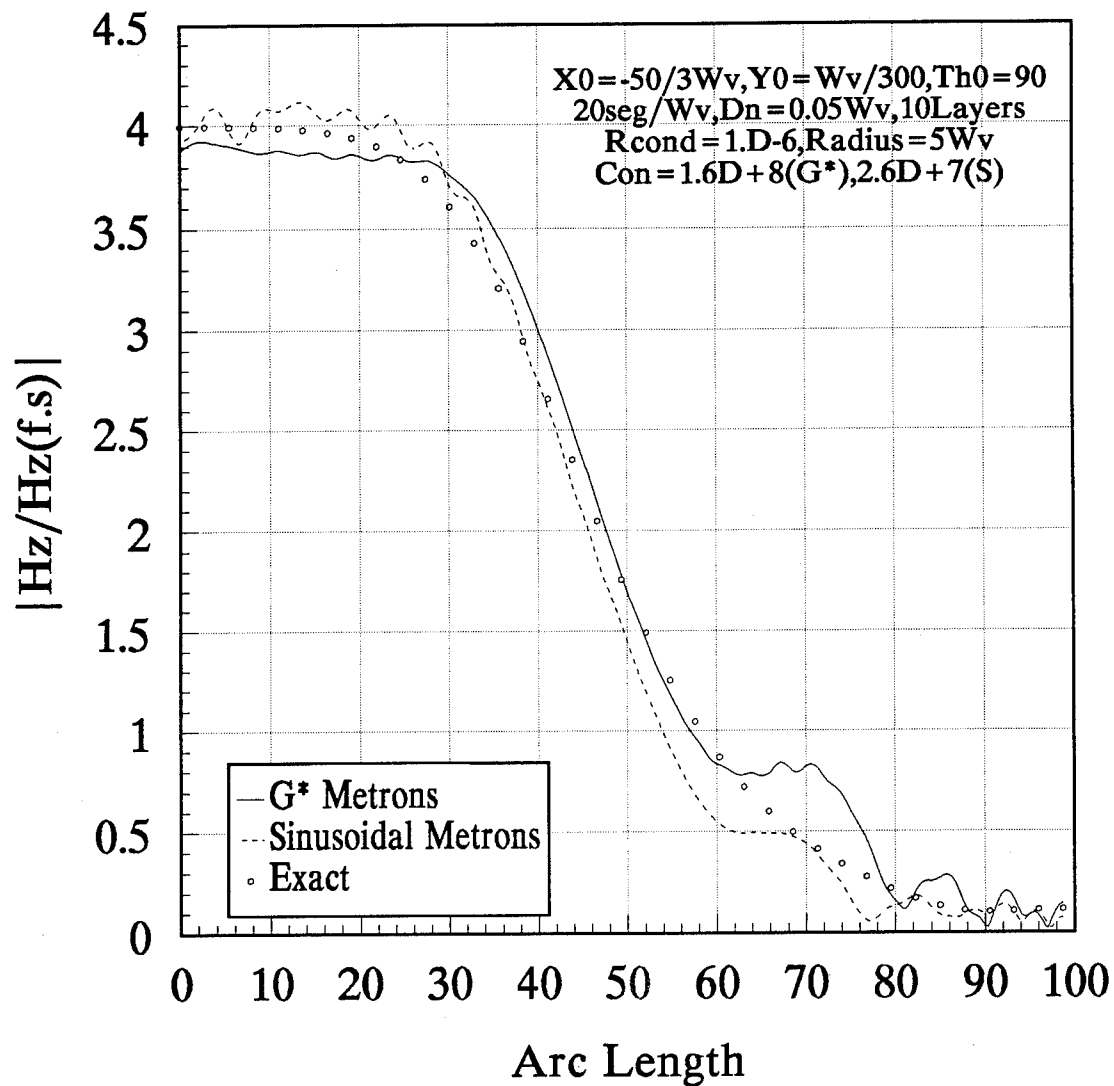


FIG. 19.

Surface Magnetic Field on Circular Boss

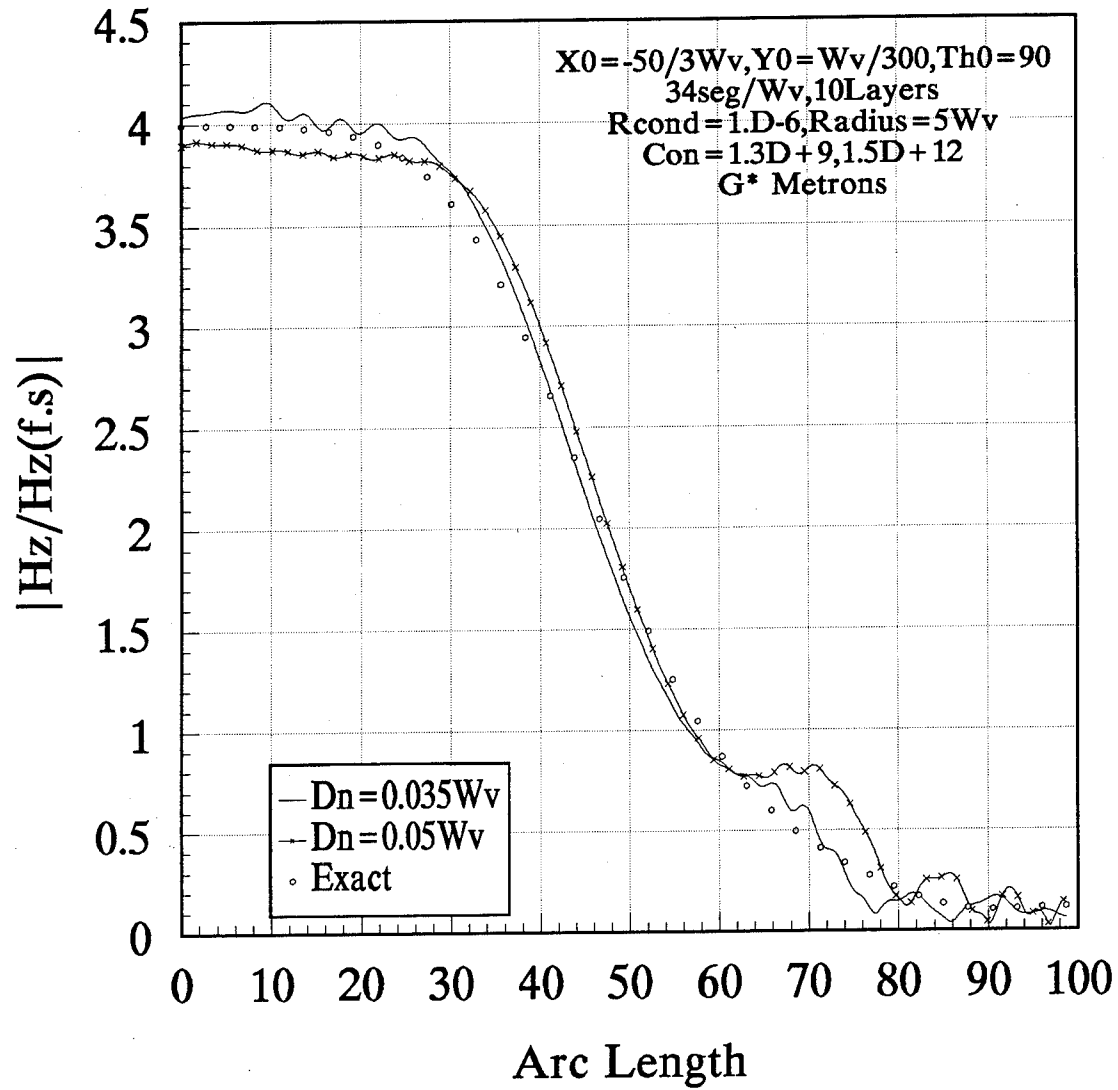


FIG. 20.

Surface Magnetic Field on Circular Boss

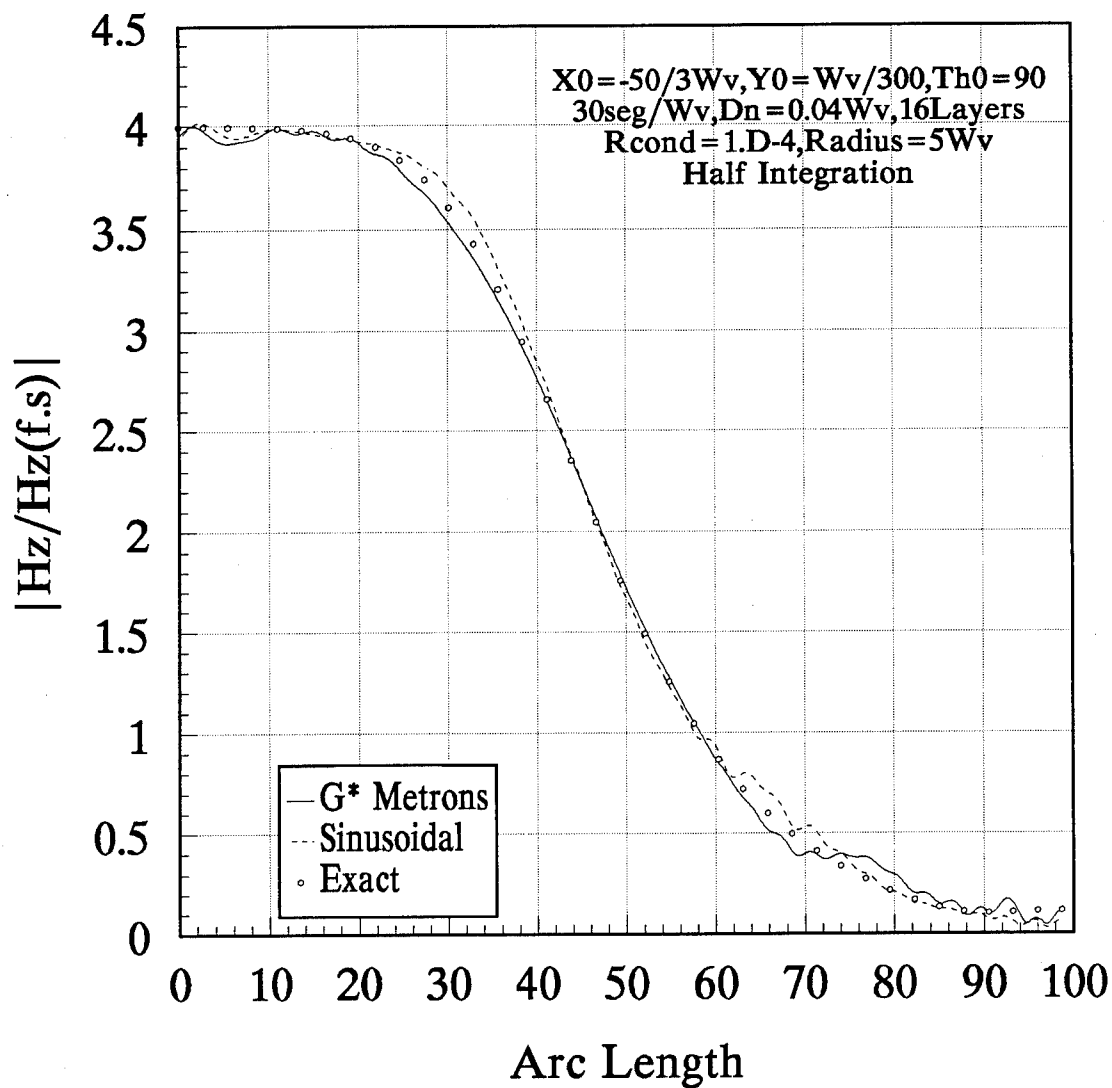


FIG. 21.

Incident Magnetic Field on Surface

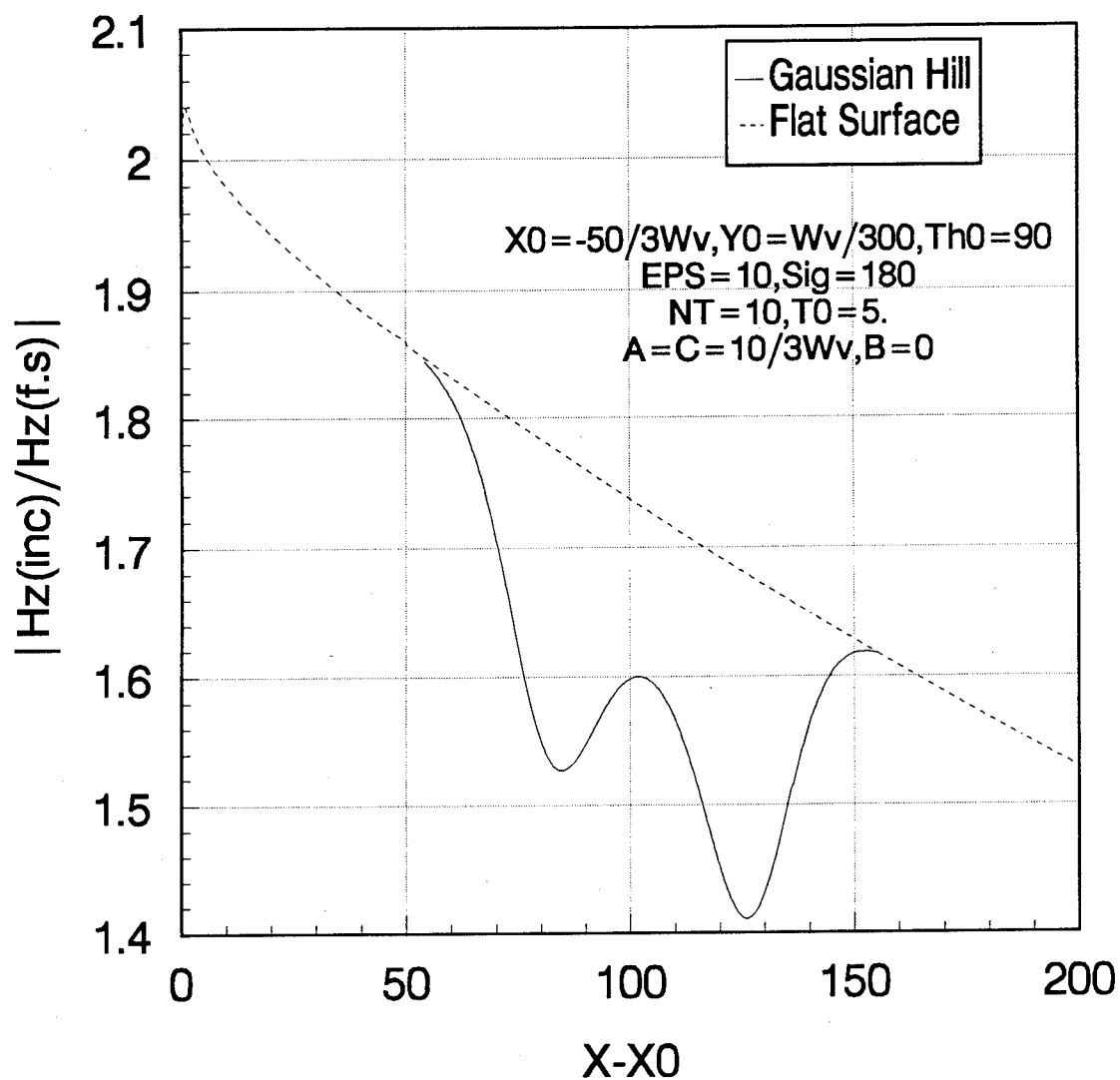


FIG. 22.

Surface Magnetic Field on Gaussian Hill

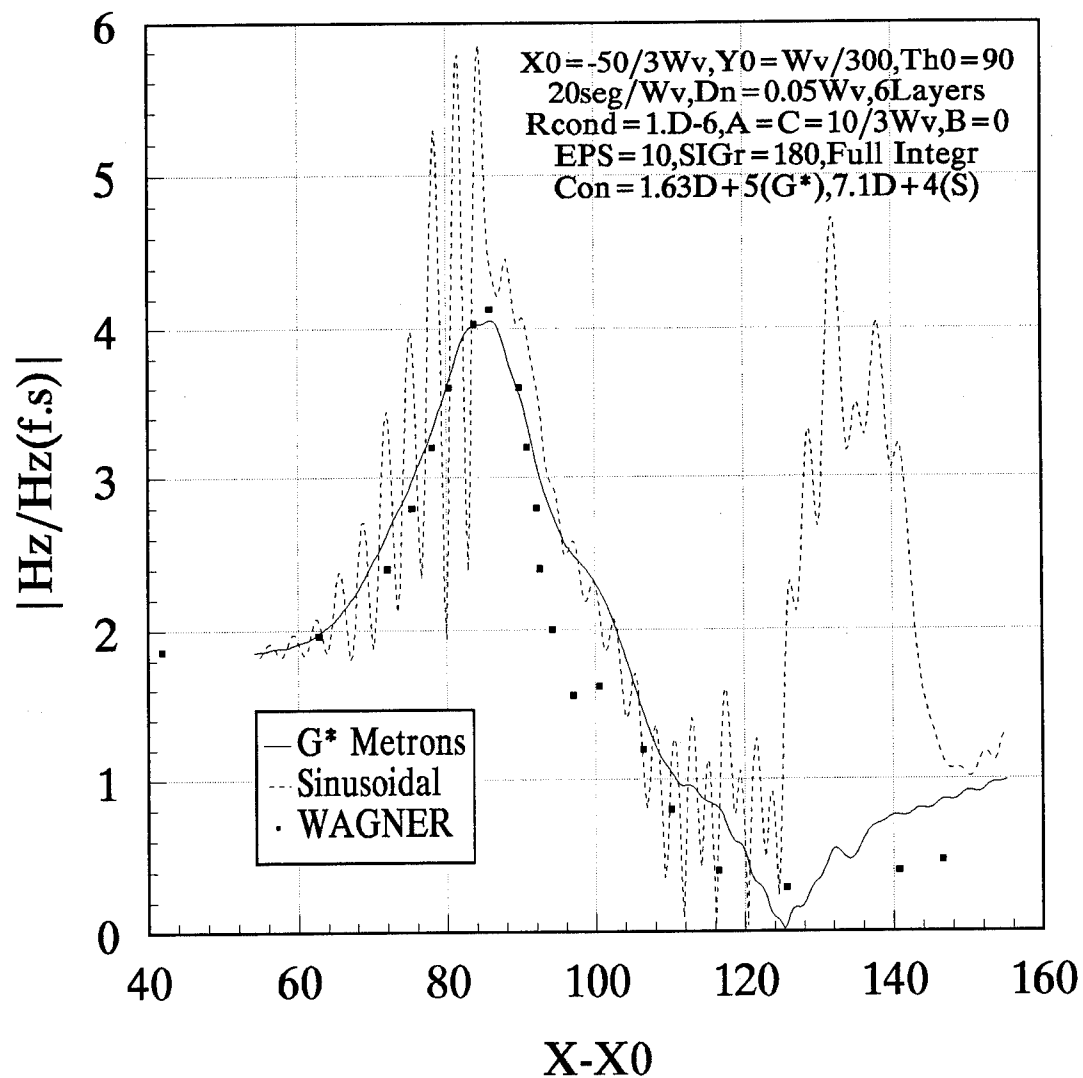


FIG. 23.

Surface Magnetic Field on Gaussian Hill

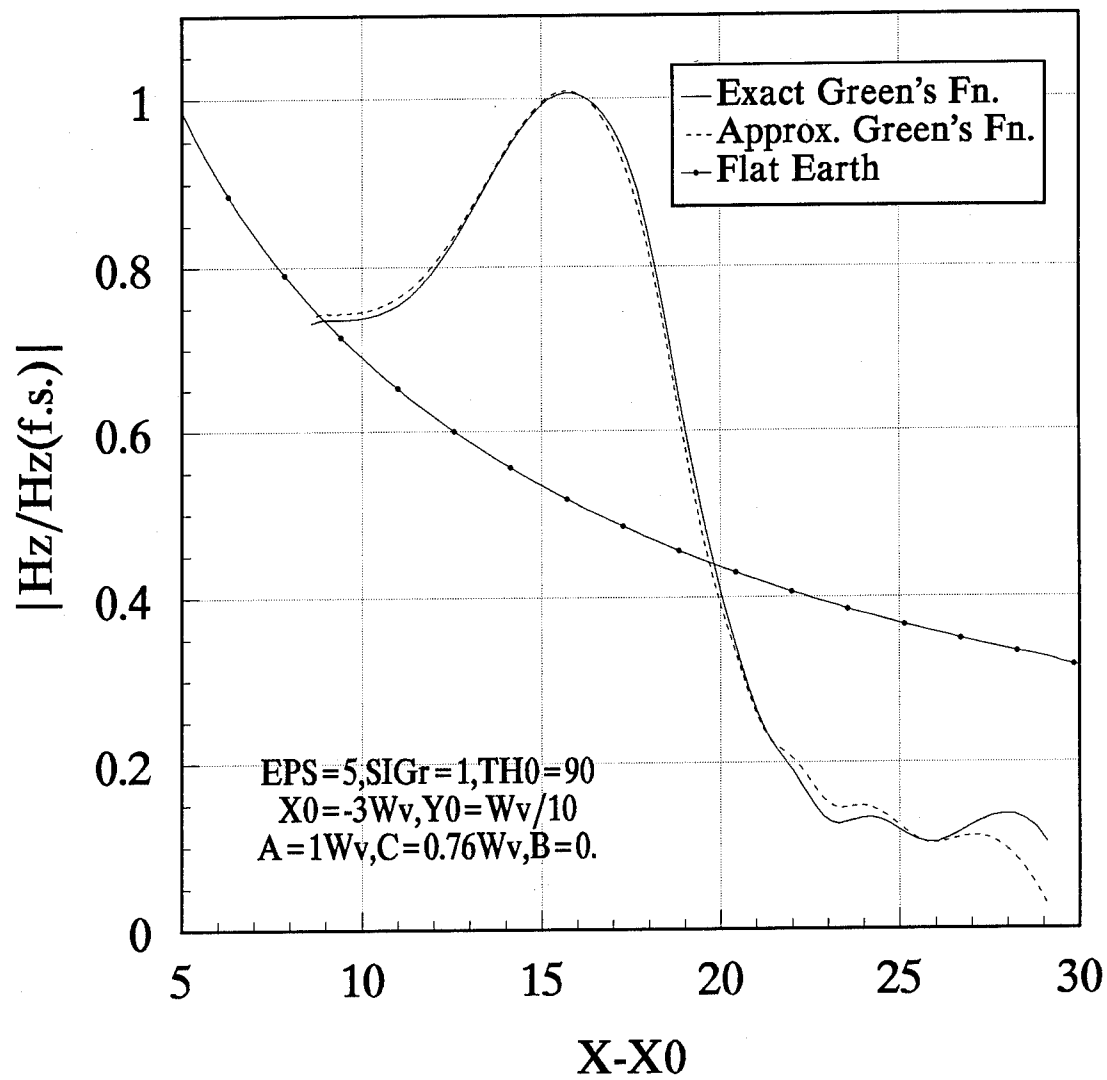


FIG. 24.

Surface Magnetic Field on Gaussian Hill

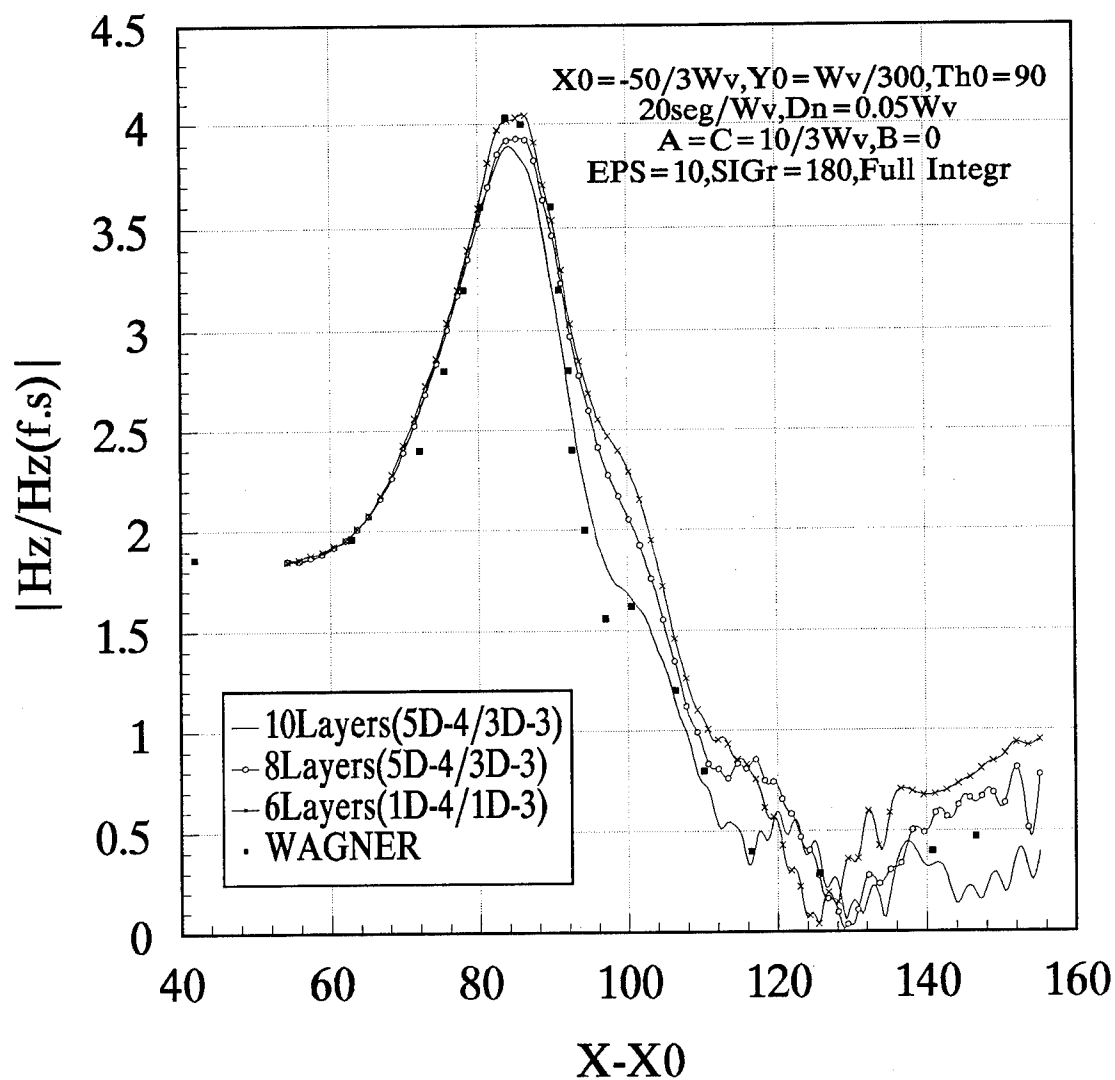


FIG. 25.

Pattern of Vertical Source Near Gaussian Hill

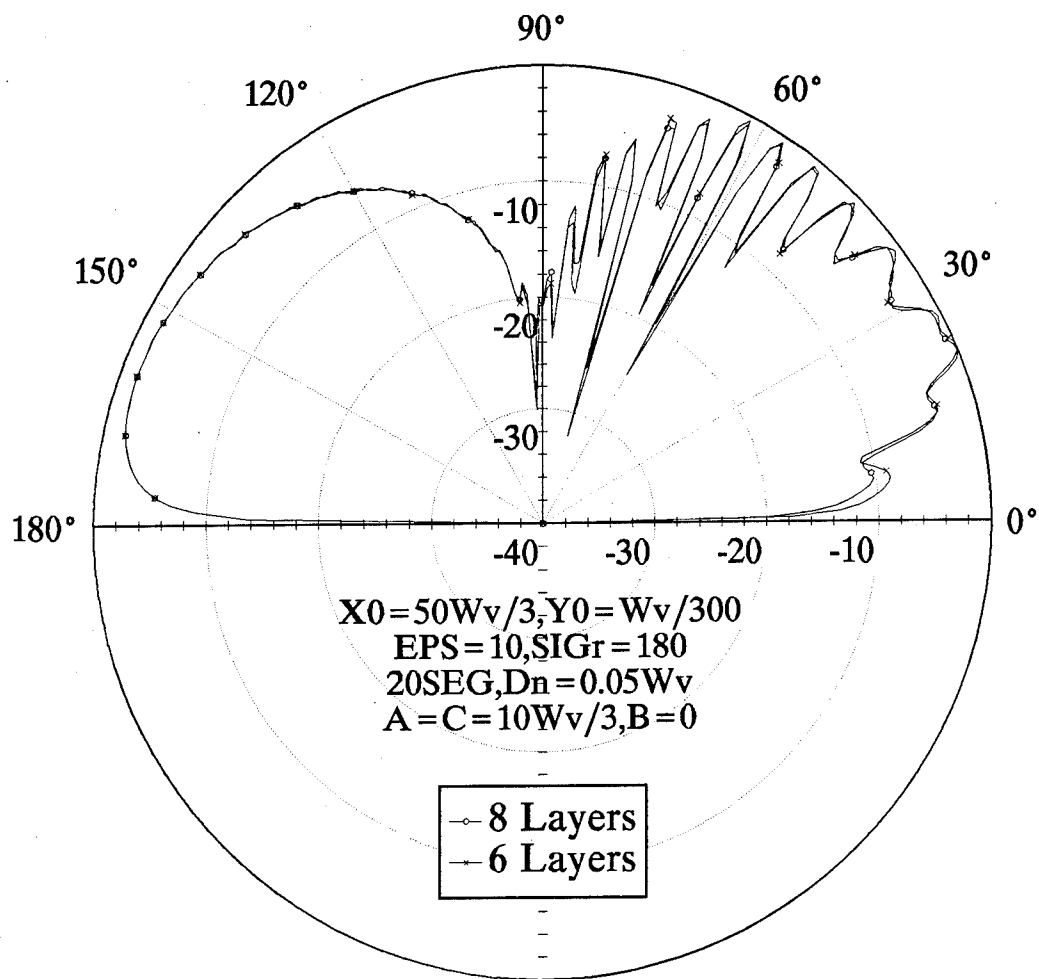


FIG. 26.

Surface Magnetic Field on Gaussian Hill

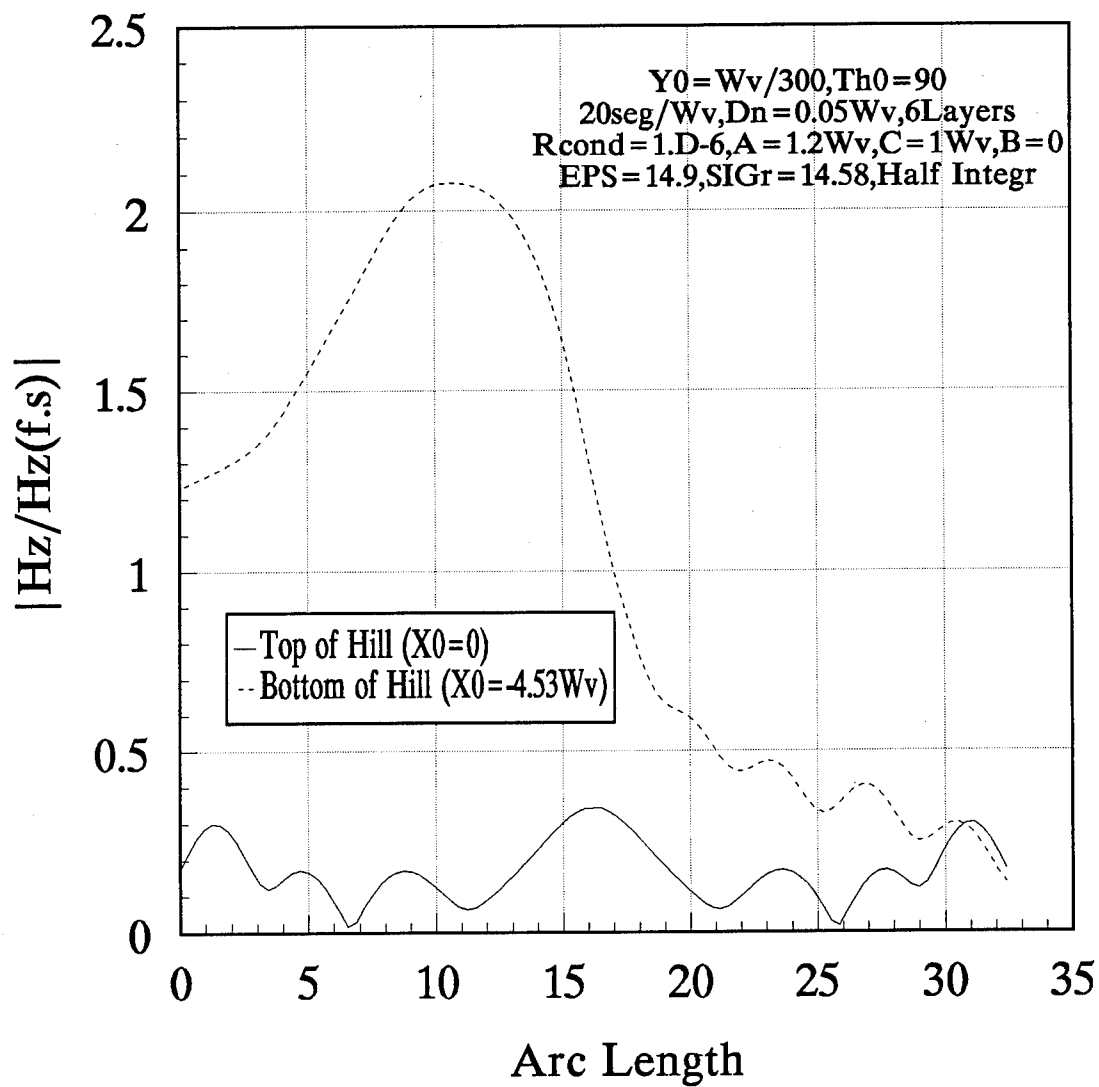


FIG. 27.

Pattern of Vertical Source Near Gaussian Hill

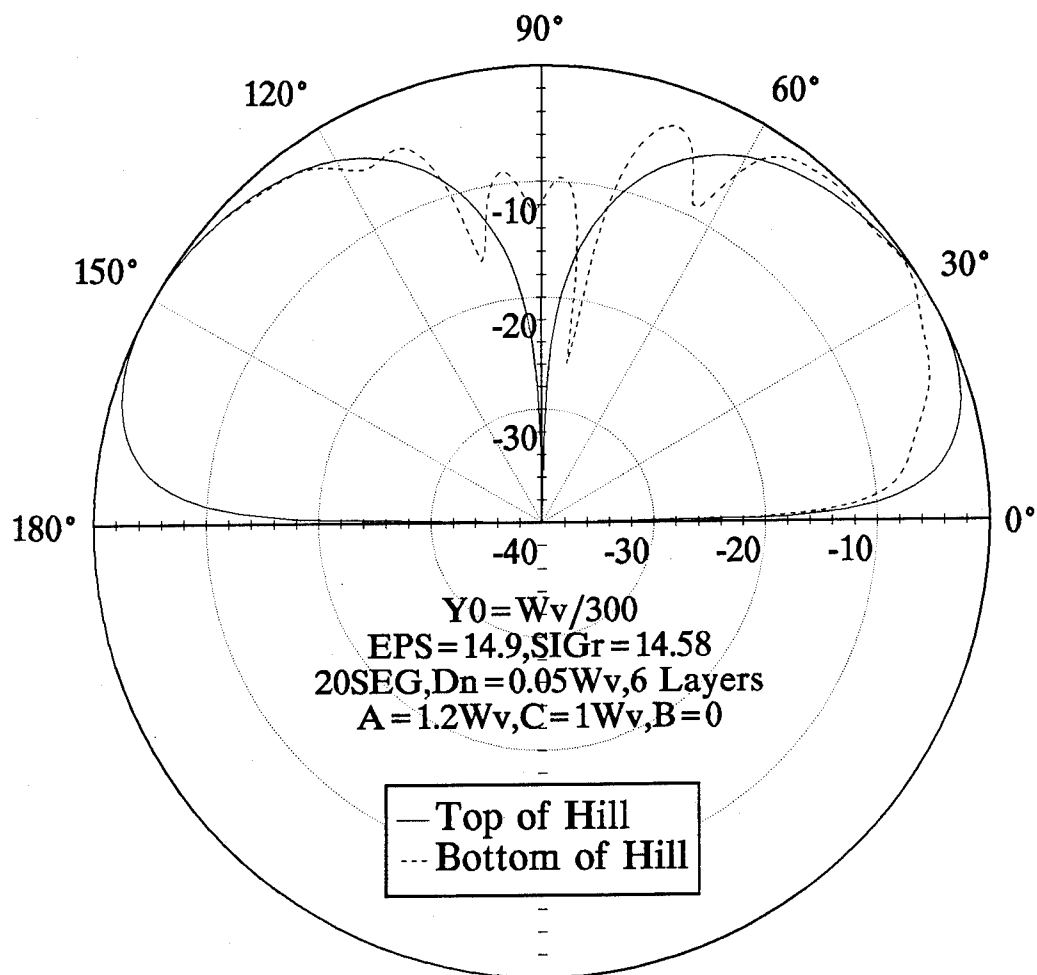


FIG. 28.

INITIAL DISTRIBUTION LIST

	No. Copies
1. Defense Technical Information Center Cameron Station Alexandria, VA 22314-6145	2
2. Dudley Knox Library, Code 52 Naval Postgraduate School Monterey, CA 93943-5002	2
3. Chairman, Code EC Department of Electrical and Computer Engineering Naval Postgraduate School 833 Dyer Road, Room 437 Monterey, CA 93943-5121	1
4. Professor Ramakrishna Janaswamy, Code EC/Js Department of Electrical and Computer Engineering Naval Postgraduate School Monterey, CA 93943-5121	10
5. LCDR Gus. K. Lott, Code Gx Naval Security Group Support Activity 3801 Nebraska Avenue NW Washington DC 20393-5220	5
6. Dr. Felix Schwering AMSEL-RD-C3-TA1 Center for C3 Systems Fort Monmouth, NJ 07703	1
7. Joseph A. Mosko Distinguished NWC Fellow Code C28203 NAWC-WPDn China Lake, CA 93556-6001	1
8. Dr. Robert Lee Assistant Professor Department of Electrical Engineering 2015 Neil Avenue Ohio State University Columbus, OH 43210-1272	1

	No. Copies
9 Brett F. Martin Naval Command, Control, and Ocean Surveillance Center NRaD, Code 536 San Diego, CA 92152	1
10 Dr. Rafael Pous Dept. of Signal Theory and Communications Universitat Politècnica De Catalunya P.O. Box 30002 08080 Barcelona, Spain	1
11 Dr. Jorgen Bach Andersen Brunstedvej 3, DK-9260 Gistrup Denmark	1
12 Professor K. K. Mei EECS Department University of California at Berkeley 207-196 Cory Hall Berkeley, CA 94720	1
13 Dr. L. S. Tamil Eric Jonsson School of Engineering University of Texas at Dallas P.O. Box 830688, MP 32 Richardson, TX 75083-0688	1
14 Daniel W. Drago Vice President, Advanced Development Government Electronics Division California Microwave, Inc. P.O. Box 2800 8022 Variel Avenue Woodland Hills, CA 91367	1
15 Richard C. Dempsey Manager, Advanced Antenna Systems Government Electronics Division California Microwave, Inc. P.O. Box 2800 8022 Variel Avenue Woodland Hills, CA 91367	1

No. Copies

1

16. Professor Richard Adler, Code EC/Ab
Department of Electrical and Computer Engineering
Naval Postgraduate School
Monterey, CA 93943-5121

1

17. Dr. G. J. Burke
Engineering Research Division
Lawrence Livermore National Laboratory
University of California
P.O. Box 5504, L-156
Livermore, CA 94550